The role of topography and lateral velocity heterogeneities on near-source scattering and ground-motion variability

Author(s):
Imperatori, W.; Mai, P.M.

Publication date:
2015-09

Permanent link:
https://doi.org/10.3929/ethz-b-000103890

Originally published in:
Geophysical Journal International 202(3), https://doi.org/10.1093/gji/ggv281

Geophysical Journal International

Geophys. J. Int. (2015) **202,** 2163–2181 doi: 10.1093/gji/ggv281
GJI Seismology

The role of topography and lateral velocity heterogeneities on near-source scattering and ground-motion variability

W. Imperatori[1] and P.M. Mai[2]

[1]*Swiss Seismological Service, Eidgenössische Technische Hochschule (ETH) Zürich, Sonneggstrasse 5, CH-8092 Zurich, Switzerland. E-mail: imperatori@tomo.ig.erdw.ethz.ch*
[2]*Division of Physical Sciences and Engineering, KAUST, Thuwal 23955-6900, Kingdom of Saudi Arabia*

Accepted 2015 June 29. Received 2015 June 16; in original form 2014 September 26

SUMMARY

The scattering of seismic waves travelling in the Earth is not only caused by random velocity heterogeneity but also by surface topography. Both factors are known to strongly affect ground-motion complexity even at relatively short distance from the source. In this study, we simulate ground motion with a 3-D finite-difference wave propagation solver in the 0–5 Hz frequency band using three topography models representative of the Swiss alpine region and realistic heterogeneous media characterized by the Von Karman correlation functions. Subsequently, we analyse and quantify the characteristics of the scattered wavefield in the near-source region. Our study shows that both topography and velocity heterogeneity scattering may excite large coda waves of comparable relative amplitude, especially at around 1 Hz, although large variability in space may occur. Using the single scattering model, we estimate average Q_C values in the range 20–30 at 1 Hz, 36–54 at 1.5 Hz and 62–109 at 3 Hz for constant background velocity models with no intrinsic attenuation. In principle, envelopes of topography-scattered seismic waves can be qualitatively predicted by theoretical back-scattering models, while forward- or hybrid-scattering models better reproduce the effects of random velocity heterogeneity on the wavefield. This is because continuous multiple scattering caused by small-scale velocity perturbations leads to more gentle coda decay and envelope broadening, while topography abruptly scatters the wavefield once it impinges the free surface. The large impedance contrast also results in more efficient mode mixing. However, the introduction of realistic low-velocity layers near the free surface increases the complexity of ground motion dramatically and indicates that the role of topography in elastic waves scattering can be relevant especially in proximity of the source. Long-period surface waves can form most of the late coda, especially when intrinsic attenuation is taken into account. Our simulations indicate that both topography and velocity heterogeneity scattering may result in large ground-motion variability, characterized by standard deviation values in the range 0.2–0.5 also at short distance from the source. We conclude that both topography and velocity heterogeneity should be considered to correctly assess the ground-motion variability in earthquake scenario studies even at intermediate frequency.

Key words: Earthquake ground motions; Computational seismology; wave propagation.

1 INTRODUCTION

Ground-motion complexity plays an important role in the context of seismic hazard assessment. Within a few fault lengths and at frequencies of engineering interest, the ground-shaking history strongly depends on fault geometry, the detailed rupture processes, seismic wave-propagation and local site effects. As a direct consequence large variability of ground motion is found for intensity measures such as peak ground acceleration (PGA) or peak ground velocity (PGV), as observed in recordings from sites close to the active fault (e.g. 1999 Chi-Chi, Taiwan, 2000 Tottori, Japan and 2004 Parkfield, California).

In the last decade, there has been an increasing usage in earthquake engineering of broad-band time-series of strong ground motion as input to model buildings as complex, dynamic, nonlinear multi-degree-of-freedom system. This, together with significant advances in the understanding of fault rupture processes, wave propagation phenomena, and site response characterization, has fostered the development of various hybrid techniques to compute synthetic seismograms for earthquake scenario purposes (e.g. Liu *et al.* 2006;

Graves & Pitarka 2010; Mai *et al.* 2010; Imperatori & Mai 2012). At frequencies above 1 Hz, techniques are generally based upon a stochastic representation of source radiation combined with a simplified theoretical representation of wave propagation and scattering effects.

However, with the fast growth in computational power, it is becoming feasible to deterministically investigate both rupture and propagation phenomena at increasingly higher frequency (e.g. Pitarka 2009; Hartzell *et al.* 2010; Dunham *et al.* 2011; Imperatori & Mai 2013; Shi & Day 2013).

In the present study, we focus on the effects of topography and random velocity heterogeneity on near-source ground motion. Here we use the term near-source to indicate a separation distance from the source generally shorter than 50 km. The importance of topography on ground shaking has been documented in a number of studies using observed records of past earthquakes (Spudich *et al.* 1996; Assimaki *et al.* 2005) and numerical simulations (Geli *et al.* 1988; Bouchon *et al.* 1996; Komatitsch *et al.* 2004; Zhang *et al.* 2008, among others). Topography is known to play a fundamental role also in volcanic regions (O'Brien & Bean 2009; Anderson *et al.* 2012). Recently, particular attention was paid to the effects that topography has on nearby low-lying areas such as basins (Ma *et al.* 2007; Lee *et al.* 2009). These studies have shown that the amplitude of shaking at the top of hills and ridges can be significantly larger than at the bases of hills or on level surfaces. Two classical examples are represented by the strong amplifications recorded at the Pacoima Dam site during the San Fernando earthquake (M_w 6.5, 1971) and at the Tarzana site during the Northridge earthquake (M_w 6.7, 1994): the first site was located on a sharp ridge, while the second on a flat, broad hill. Moreover, macroscopic topographic features can either reduce or increase ground-motion amplitude in nearby basins depending on source position and rupture process (Lee *et al.* 2009), with multiple reflections prolonging seismic shaking (Lee *et al.* 2008).

On the other hand, velocity heterogeneities in the Earth crust are responsible of intense seismic waves scattering, resulting in coda waves widely documented in recorded time-series (Aki 1969; Sato & Fehler 1998), envelope broadening (Sato 1989) and variations in waveform, amplitude and traveltime across nearby receivers (Flatté & Wu 1988; Zerva & Zervas 2002). Many theories have been developed to explain the nature of coda waves (e.g. Aki & Chouet 1975; Wu 1985; Zeng *et al.* 1991). Eventually, the scattering of elastic waves has become the subject of a series of studies applying deterministic and stochastic modelling (Frankel & Clayton 1986; Roth & Korn 1993; Saito *et al.* 2002; Nielsen & Thybo 2003; Pitarka 2009), targeted towards a deeper understanding of the scattering process, and deciphering the characteristics and distribution of heterogeneities in the Earth crust and mantle. Recently, Imperatori & Mai (2013) have demonstrated that scattering can sensibly increase ground-motion complexity already at few kilometres away from the source, where source effects were generally thought to dominate (Guatteri *et al.* 2003; Aagaard & Heaton 2004; Ripperger *et al.* 2008).

As shown by Bouchon *et al.* (1996) and Lee *et al.* (2009), topography can scatter travelling waves and radiate diffracted body and surface waves, analogously to velocity heterogeneity. O'Brien & Bean (2009) and Kumagai *et al.* (2011) have conducted broadband numerical simulations of scattering from the topography and internal volcanic structure and found that topography appears to be the dominant scatterer in most cases.

In this work we analyse and compare the effects of topography and random velocity heterogeneity on the wave-field at short and intermediate distance from the source ($R < 50$ km), paying particular attention to coda waves and ground-motion variability. We explore ground motion in the 0–5 Hz frequency range using 3-D numerical simulations, considering rough topography models with different characteristics and realistic random velocity models representing the heterogeneous nature of the upper crust (Imperatori & Mai 2013). We also test the hypothesis whether topography scattering could be used as a proxy for velocity heterogeneity scattering. If this conjecture is found to be true, engineering-oriented ground-motion simulations that include seismic wave scattering would become simpler because Earth topography is well known while the 3-D small-scale heterogeneous Earth structure is not.

2 TOPOGRAPHY AND 3-D VELOCITY MODELS

In this study, we consider three different topographies representing typical alpine and foreland areas in Switzerland. As shown in Fig. 1, each of them contains particular characteristics. Model T1 (left) features large high peaks and a pronounced valley in the lower-right corner (Rhône valley, SW Switzerland); model T2 (centre) is asymmetrical, with altitude and topography roughness increasing towards the lower side (Swiss plateau); model T3 (right) is more uniform and presents crests alternating with deep troughs of different orientation (Engadin region, SE Switzerland). In particular, model T3 presents spatial features of shorter wavelength compared to the other two models.

Heterogeneous 3-D velocity models can be obtained by superimposing a spatial random field to a specific deterministic model, as described in Imperatori & Mai (2013). The random field is represented by a Von Karman power spectral density function, whose correlation length, Hurst exponent and standard deviation control the characteristics of the velocity perturbations. On the basis of borehole investigations (e.g. Holliger 1997; Dolan *et al.* 1998) and recent numerical simulations (e.g. Hartzell *et al.* 2010; Imperatori & Mai 2013), we set these parameters to 3 km, 0.3 and 7.5 per cent, respectively. According to Takemura & Furumura (2013), these can be considered as average values for the upper crust. The initial background shear wave speed is constant and equal to 3000 m s^{-1}, but subsequently, we superpose a depth-dependent wave-speed profile.

Fig. 1 shows a map view of the three heterogeneous models (labelled H1, H2 and H3) used in our study. All models have identical spectral characteristics but are initialized with different seed number. In these models the free surface, although flat, is not placed at reference level $z = 0$ but at the average elevation of the corresponding T-model. Therefore, for model H1 the free surface lies at $z = 1575$ m, for model H2 at $z = 1097$ m, and for model H3 at $z = 2156$ m. This ensures that the average hypocentral distance remains the same between two corresponding models.

Together with the heterogeneous models above, we consider also three unperturbed media with flat free surface (R1, R2 and R3), which will serve as reference models. A list of the models, including their main characteristics, is given in Table 1.

Homogeneous background velocity models can be useful to study fundamental characteristics of topography and heterogeneity scattering, but they lack vertical layering and velocity gradients commonly present in 1-D velocity models of the Earth crust. These deterministic features alone are able to enhance ground-motion complexity. Moreover, as shown by Pitarka (2009) and Imperatori & Mai (2013), low-velocity layers close to the free surface can strongly affect the scattering of seismic waves. We

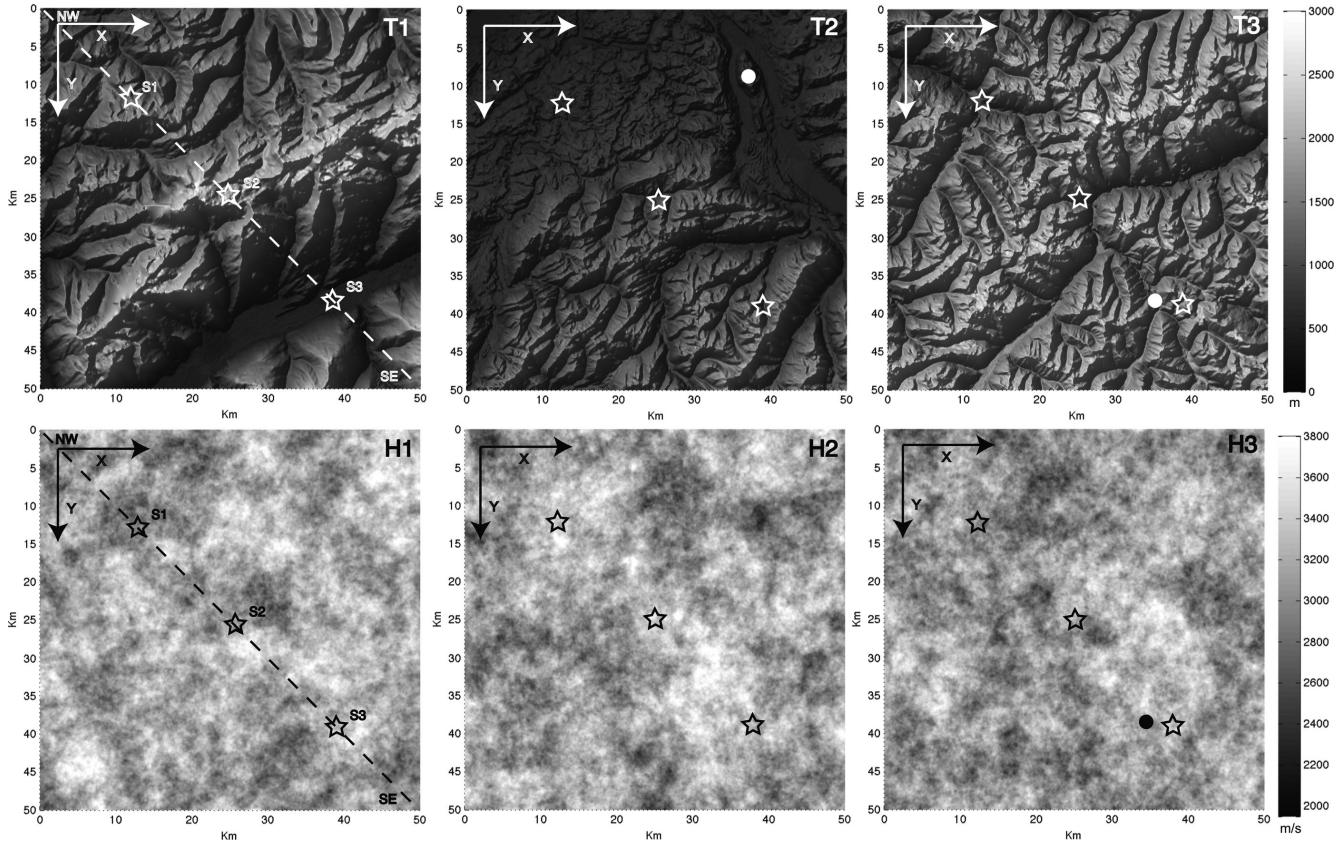

Figure 1. Top row: topography models used in this study. Colour scale indicates elevation above sea level. Models are referred as to (left to right) T1, T2 and T3. Bottom row: map view of the 3-D heterogeneous velocity models used in this study. Colour scale indicates shear wave speed. Models are referred to as (left to right) H1, H2 and H3. In both rows, stars show the three epicentres S1, S2 and S3, while circles represent the position of the array used to compute vespagrams in Fig. 9.

therefore introduce a fourth set of models where the background shear wave speed is depth-dependent. Due to high computational costs, we introduce this new feature only for models R3, T3 and H3. We choose this particular set of models since T3 has the roughest topography and, therefore, the largest scattering potential. Following available studies for the alpine region in Switzerland (Husen *et al.* 2003; Steimen *et al.* 2003; Roten *et al.* 2008), we adopt the 1D velocity model shown in Fig. 2. This model is characterized by a low-velocity layer overlying a 2 km thick region with a linear velocity gradient. The minimum shear wave speed is 2300 m s^{-1}, a typical value for bedrock at shallow depths in the area under study (Steimen *et al.* 2003). The resulting new models are indicated by the letter L (e.g. T3L).

All the models introduced so far are purely elastic. However, while anelastic attenuation (i.e. absorption) can be neglected in presence of high-velocity materials at short and moderate distance, the introduction of low-velocity layers requires visco-elastic modelling to simulate realistic wave propagation (e.g. Olsen *et al.* 2003). We set attenuation as follows: for z above mean sea level (i.e. 0 km), $Q_S = 40$, for z between 0 and -2 km (corresponding to the velocity gradient of our 1-D model) $Q_S = 100$, for z below -2 km $Q_S = 300$. Q_P is approximated as $\frac{9}{4}Q_S$. These values are in agreement with those proposed by Steimen *et al.* (2003), Oprsal *et al.* (2005) and Bethmann *et al.* (2012) for the Siwss region. We refer to these new models as R3LQ, T3LQ and H3LQ.

In all our models, the V_p/V_s ratio is set to $\sqrt{3}$, while density estimates are obtained using the empirical relation proposed by Brocher (2005).

3 SOURCE REPRESENTATION AND NUMERICAL MODELLING

We deploy three point-like shear dislocations placed at $x\,(=y) = 12.5$ km (S1), $x\,(=y) = 25$ km (S2) and $x\,(=y) = 37.5$ km (S3), all located at depth $z = -5$ km (see Figs 1–3). These sources are characterized by a right-lateral strike-slip mechanism with a strike value of 30°. The source time function is a smoothed version of the Brune function (Brune 1970), presenting three continuous derivatives at $t = 0$:

$$g(t,\omega) = \begin{cases} 0 & t < 0 \\ 1 - \mathrm{e}^{-\omega t}[1 + \omega t + \frac{1}{2}(\omega t)^2 - \frac{3}{2x_0}(\omega t)^3 & \\ \quad + \frac{2}{2x_0{}^2}(\omega t)^4 - \frac{1}{2x_0{}^3}(\omega t)^5] & 0 < \omega t < x_0 \\ 1 - \mathrm{e}^{-\omega t}(1 + \omega t) & \omega t > x_0 \end{cases} \quad (1)$$

where $x_0 = 2.31$. The smoothed Brune is similar to the standard Brune's ω^2-model, but has a faster fall-off at high frequency, thus reducing the risk of frequency aliasing when analysing time snapshots of the wave field at the free surface.

The source time-function parameter ω is fixed such that the corner frequency is 1.0 Hz. Following Allmann & Shearer (2009), it corresponds to a moment magnitude M_w of 5.0.

In this study, we conduct numerical simulations with the second-order finite-difference code WPP of Nilsson *et al.* (2007). The numerical method is based on summation by part stencils, featuring efficient absorbing boundaries, vertical mesh refinement and

Table 1. Summary and main features of the models used in this study. We deployed a point-source at three different locations for all models. See the text for details.

Model	Free-surface	Background velocity	Velocity heterogeneity	Model material
R1	flat, z = 1575 m	Vs = 3000 m s^{-1}	NO	elastic
R2	flat, z = 1097 m	Vs = 3000 m s^{-1}	NO	elastic
R3	flat, z = 2156 m	Vs = 3000 m s^{-1}	NO	elastic
T1	irregular	Vs = 3000 m s^{-1}	NO	elastic
T2	irregular	Vs = 3000 m s^{-1}	NO	elastic
T3	irregular	Vs = 3000 m s^{-1}	NO	elastic
H1	flat, z = 1575 m	Vs = 3000 m s^{-1}	YES	elastic
H2	flat, z = 1097 m	Vs = 3000 m s^{-1}	YES	elastic
H3	flat, z = 2156 m	Vs = 3000 m s^{-1}	YES	elastic
R3L	flat, z = 2156 m	Vs = 2300 m s^{-1}, $z > 0$ km 2300 m s^{-1} < Vs < 3500 m s^{-1}, 0 < z < –2 km Vs = 3500 m s^{-1}, z < –2 km	NO	elastic
T3L	irregular	Vs = 2300 m s^{-1}, $z > 0$ km 2300 m s^{-1} < Vs < 3500 m s^{-1}, 0 < z < –2 km Vs = 3500 m s^{-1}, z < –2 km	NO	elastic
H3L	flat, z = 2156 m	Vs = 2300 m s^{-1}, $z > 0$ km 2300 m s^{-1} < Vs < 3500 m s^{-1}, 0 < z < –2 km Vs = 3500 m s^{-1}, z < –2 km	YES	elastic
R3LQ	flat, z = 2156 m	Vs = 2300 m s^{-1}, $z > 0$ km 2300 m s^{-1} < Vs < 3500 m s^{-1}, 0 < z < –2 km Vs = 3500 m s^{-1}, z < –2 km	NO	visco-elastic
T3LQ	irregular	Vs = 2300 m s^{-1}, $z > 0$ km 2300 m s^{-1} < Vs < 3500 m s^{-1}, 0 < z < –2 km Vs = 3500 m s^{-1}, z < –2 km	NO	visco-elastic
H3LQ	flat, z = 2156 m	Vs = 2300 m s^{-1}, $z > 0$ km 2300 m s^{-1} < Vs < 3500 m s^{-1}, 0 < z < –2 km Vs = 3500 m s^{-1}, z < –2 km	YES	visco-elastic

visco-elastic attenuation (Petersson & Sjögreen 2012). In addition to heterogeneous material models, the code can handle complex topography by means of a curvilinear grid extending from the free surface into the computational domain to a user specified level, where it is replaced by a standard Cartesian grid. We set the grid-step to 40 and 26 m for the homogeneous and the heterogeneous models, respectively. Since accurate results are expected when at least 12–15 points per minimum wavelength are observed (Nilsson *et al.* 2007), we low-pass filter all output synthetics at 5 Hz.

Although we consider only receivers within a 50 km long squared region at the free-surface (Figs 1 and 2), the effective computational domain extends 70 km along the horizontal direction and 40 km in depth in order to dampen eventual boundary reflections. The computational time required by each simulations varies according to the grid-step, the presence of topography and intrinsic attenuation, ranging from few hours up to 16 hr on 12 288 cores of a BlueGene-P. To minimize the computational cost, we limit the maximum simulation time to 30 s if the source is placed in the centre (S2) of the models, and to 40 s otherwise (S1, S3).

Although the accuracy of WPP has been extensively tested (e.g. Rodgers *et al.* 2008), recently Galis *et al.* (2013) have shown that accurate wave propagation in highly heterogeneous media can be challenging. In particular, by investigating the response of several numerical codes (including WPP) in the presence of strong random velocity perturbations, Galis *et al.* (2013) have found that all tested methods return waveforms whose similarity decreases with frequency and epicentral distance. Based on their work, our results are expected to be robust within the frequency, distance range and velocity variability explored in the present study ($f_{max} < 5$ Hz; $R_{max} < 40$ km; $\sigma < 10$ per cent).

4 SIMULATION RESULTS

A generic overview on the simulation results is given in Figs 3 and 4, in which we show seismic profiles for several models, including those with intrinsic attenuation, at receivers located on the free surface along the dashed line represented in Fig. 1. We observe that both topography and velocity heterogeneity produce a considerable amount of scattered waves, however, with different characteristic. We first focus on the constant background velocity models (Fig. 3), as they help to illustrate the basic features of the two different

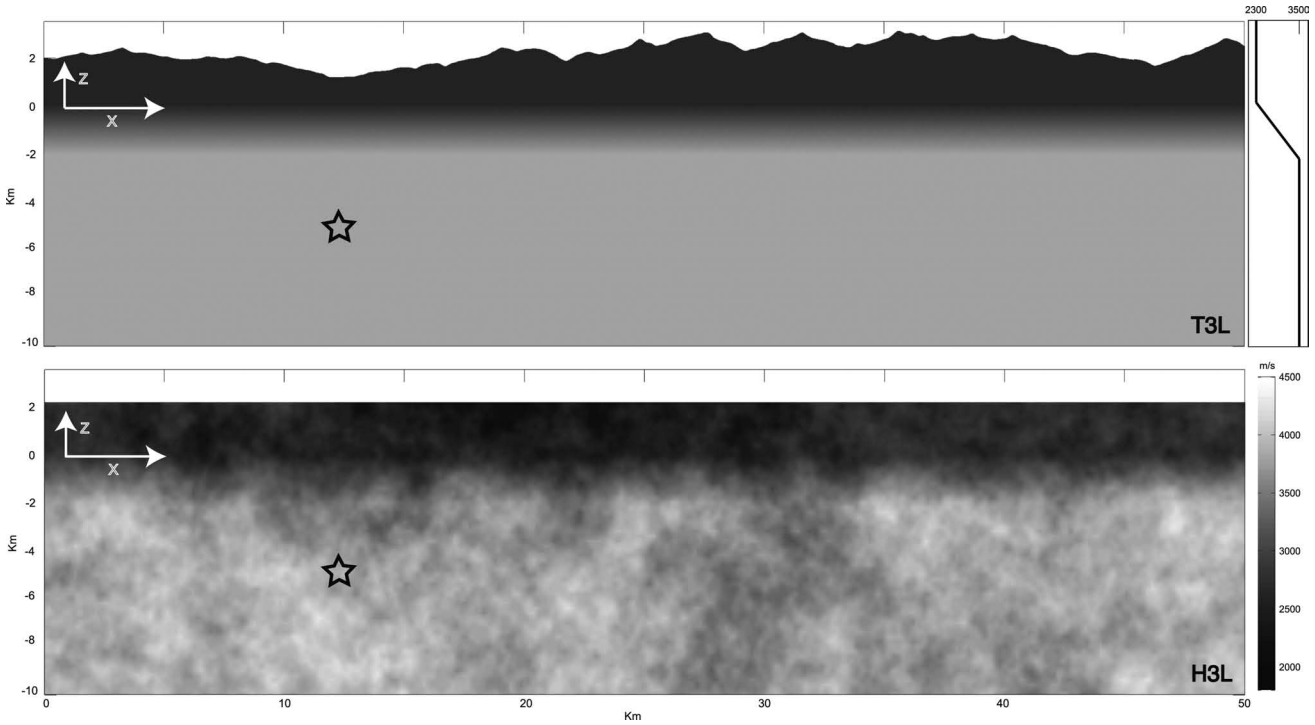

Figure 2. Vertical profiles of models T3L (top) and H3L (bottom). Profiles are parallel to the x-axis and cut the y-axis at 12.5 km. We include a schematic 1-D profile of the depth-varying background S-wave speed. The black star indicates the position of source S1. The free surface for model H3L lies at $z = 2156$ m, corresponding to the average topographic elevation in model T3. Velocity heterogeneity distribution is identical for both models H3 and H3L.

scattering mechanisms. In particular, we notice that topography scattering usually contains a direct S-wave immediately followed by large amplitude coda waves, whose amplitude drops quickly to lower levels. This observation holds for all our models independently of source position, with a partial exception in the northern part of model T2, which is characterized by very smooth topography. In this region scattered energy is more homogeneously distributed and, as seen in Fig. 3, coda waves are mainly formed by backscattered waves towards the source due to rough topography in the southern area. Our simulations thus indicate that many topographic features, depending on the source position, are very efficient in generating important secondary phases that can travel coherently across the models.

In contrast, scattering due to random velocity heterogeneity produces lower amplitude ground motion, including direct P and S waves, and more gently decaying coda waves. For these models, peak ground motion can occur well beyond the direct S wave already at about 10–20 km far from the epicentre. We conjecture that these coda characteristics can be explained by a more continuous (in space / time) scattering process that occurs as the waves travel from the source to the site through the heterogeneous medium.

Introducing a realistic background velocity distribution, characterized by a low-velocity layer overlying a velocity gradient (Fig. 2), has a strong impact on the recorded ground motion. In Fig. 4, that also includes reference models R3, RL3 and RLQ3, long-period large-amplitude surface waves dominate the seismic profiles. These waves were barely developed in the constant background velocity models (see model R3). As a result, time-series for both topography and velocity heterogeneity models now contain significant energy spread over a much larger time-span, with peak ground motion related to strong surface waves, except at very short epicentral distances ($<$10 km). The bottom row of Fig. 4 demonstrates also the dramatic effect of intrinsic attenuation, accompanied by a reduction of both ground-motion amplitude and duration. Overall, intrinsic attenuation does not seem to severely affect ground-motion complexity, although it gradually filters out high-frequency energy. This is clearly visible in Fig. 5, where we show sample velocity time-series and their spectrograms, at a receiver located on the free surface at $x = 40$ km, $y = 40$ km for a subset of models. The time-frequency analysis reveals another interesting difference between topography and velocity heterogeneity scattering: while velocity heterogeneity results in rather uniform time-series spectral signature, coda waves induced topography are gradually depleted in high-frequency energy, an effect similar to that of intrinsic attenuation to some extent. This behaviour is particularly visible in the uniform background velocity case (Fig. 5, left column) and is widely observed for all topography models, although local exceptions due to energy focusing and resonance phenomena at specific frequencies may occur. We attribute this phenomena to intense topography-induced mode conversion, described in other studies (e.g. Clouser & Langston 1995; Komatitsch & Vilotte 1998; Rodgers *et al.* 2010), resulting in long-period surface waves forming most of the late-coda, as in Fig. 4.

4.1 Coda analysis

A more quantitative analysis of the coda waves and their characteristics can be carried out by calculating the normalized root-mean-square envelope $\bar{E}_{\rm rms}(t)$, defined as:

$$\bar{E}_{\rm rms}(t) = 100 \times \frac{\sqrt{\frac{1}{n}\sum_{i=1}^{n} v_z^i(t)^2}}{\int_0^{t_{\rm max}} \sqrt{\frac{1}{n}\sum_{i=1}^{n} v_z^i(t)^2}\,{\rm d}t}, \qquad (2)$$

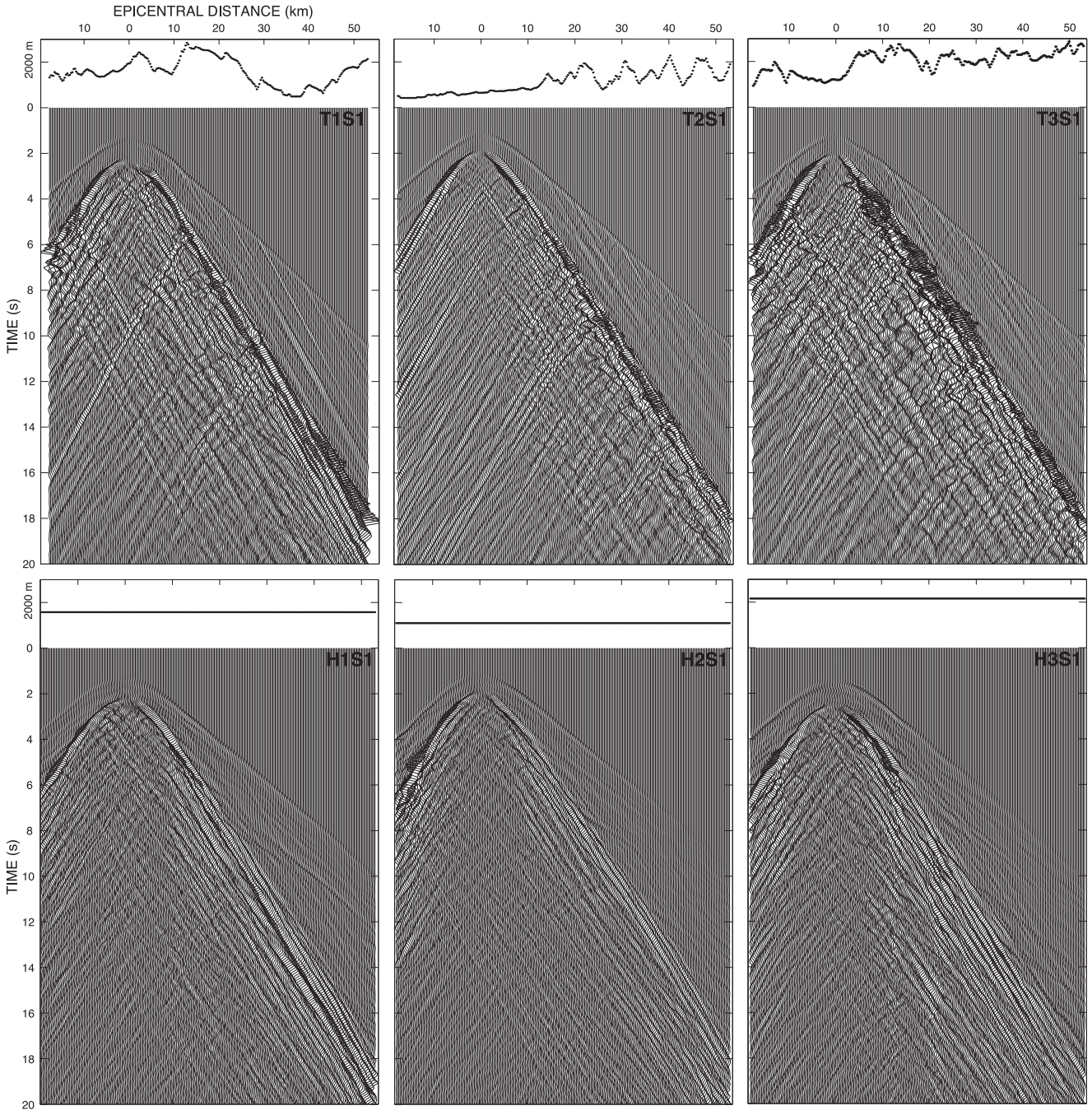

Figure 3. Top row: velocity time-series for models T1S1 (left), T2S1 (middle) and T3S1 (right). Bottom row: velocity time-series for models H1S1 (left), H2S1 (middle) and H3S1 (right). Time-series are recorded at receivers located on the free surface along the diagonal dashed line shown in Fig. 1. Only vertical component is shown. A linear time-gain is applied to each trace to compensate for geometrical spreading of travelling waves. The topography profile is reported on top. Amplitude scale is identical for all panels.

where $v_z^i(t)$ is the ith vertical velocity seismogram and n is the number of receivers at the same distance from the source. Eq. (2) expresses the relative energy content at each time sample, accounting for amplitude differences due to the continuous scattering process in the velocity heterogeneity models. Results for several models and hypocentral distances of 15 and 35 km are shown in Figs 6 and 7. Note that only receivers within the model boundary can be considered, implying some source–receiver azimuth gaps in the analysis, especially at 35 km. The $\bar{E}_{\mathrm{rms}}$ envelopes are computed by averaging over source realizations S1 and S3. For model T2, due to the strong asymmetry of the topography, the two contributions are reported separately.

Here we consider only the vertical component of motion, analogously to many Q-coda studies (e.g. Mayeda *et al.* 1992; Tuvé *et al.* 2006). Moreover, the vertical component is not affected by the large amplitude *SH* wave dominating the transversal component as a consequence of the chosen strike-slip mechanism. For the homogeneous background velocity models, the envelope analysis reveals that, at short distance from the source (Fig. 6, left column), early coda-waves generated by topography are larger than those excited

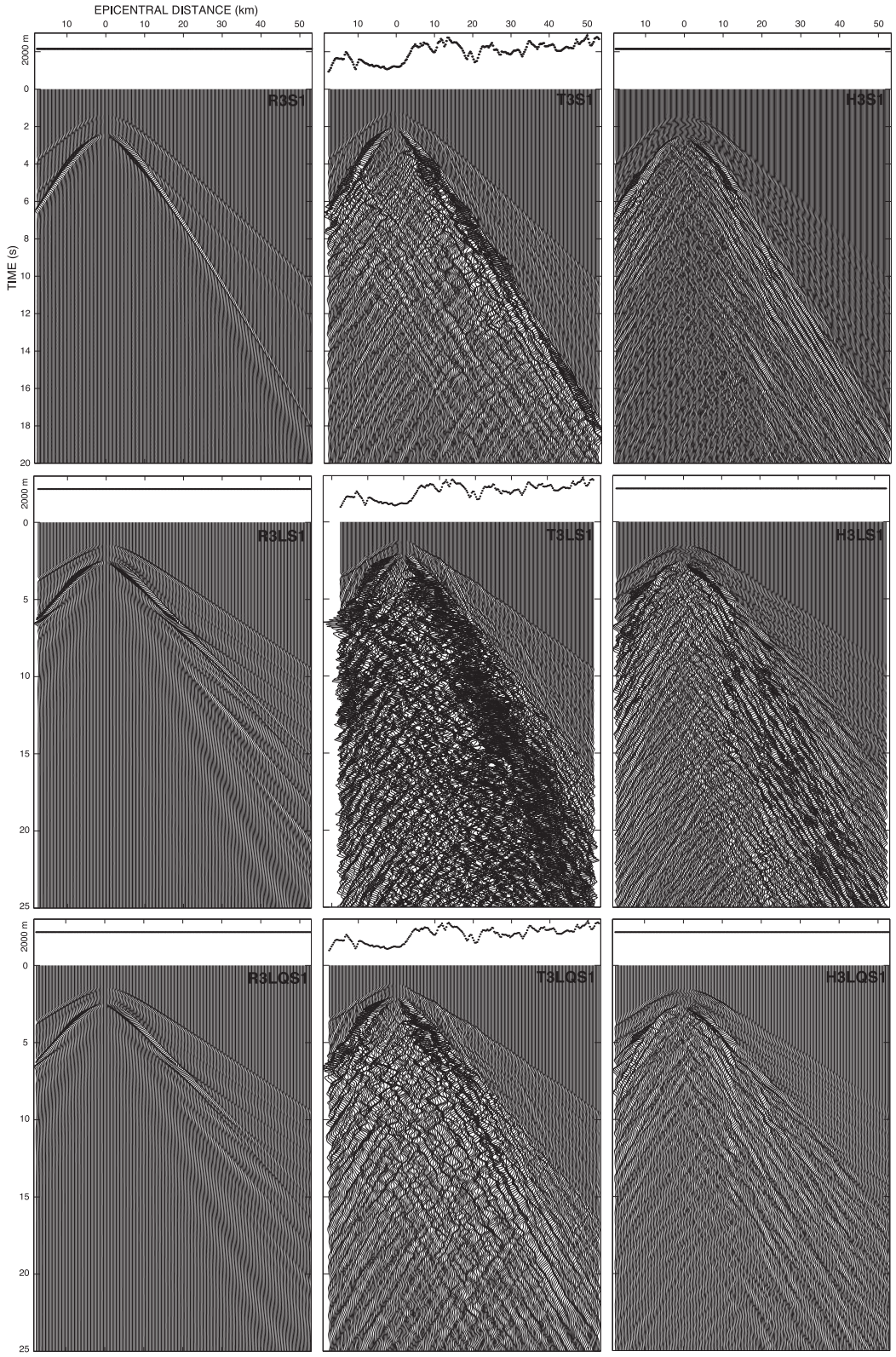

Figure 4. Top row: velocity time-series for models R3S1 (reference model, left), T3S1 (middle) and H3S1(right). Middle row: velocity time-series for models R3LS1 (reference model, left), T3LS1 (middle) and H3LS1(right). Bottom row: velocity time-series for models R3LQS1 (reference model, left), T3LQS1 (middle) and H3LQS1(right). Time-series are recorded at receivers located on the free surface along the diagonal dashed line shown in Fig. 1. Only vertical component is shown. A linear time-gain is applied to each trace to compensate for geometrical spreading of travelling waves. The topography profile is reported on top. Amplitude scale is identical for all panels.

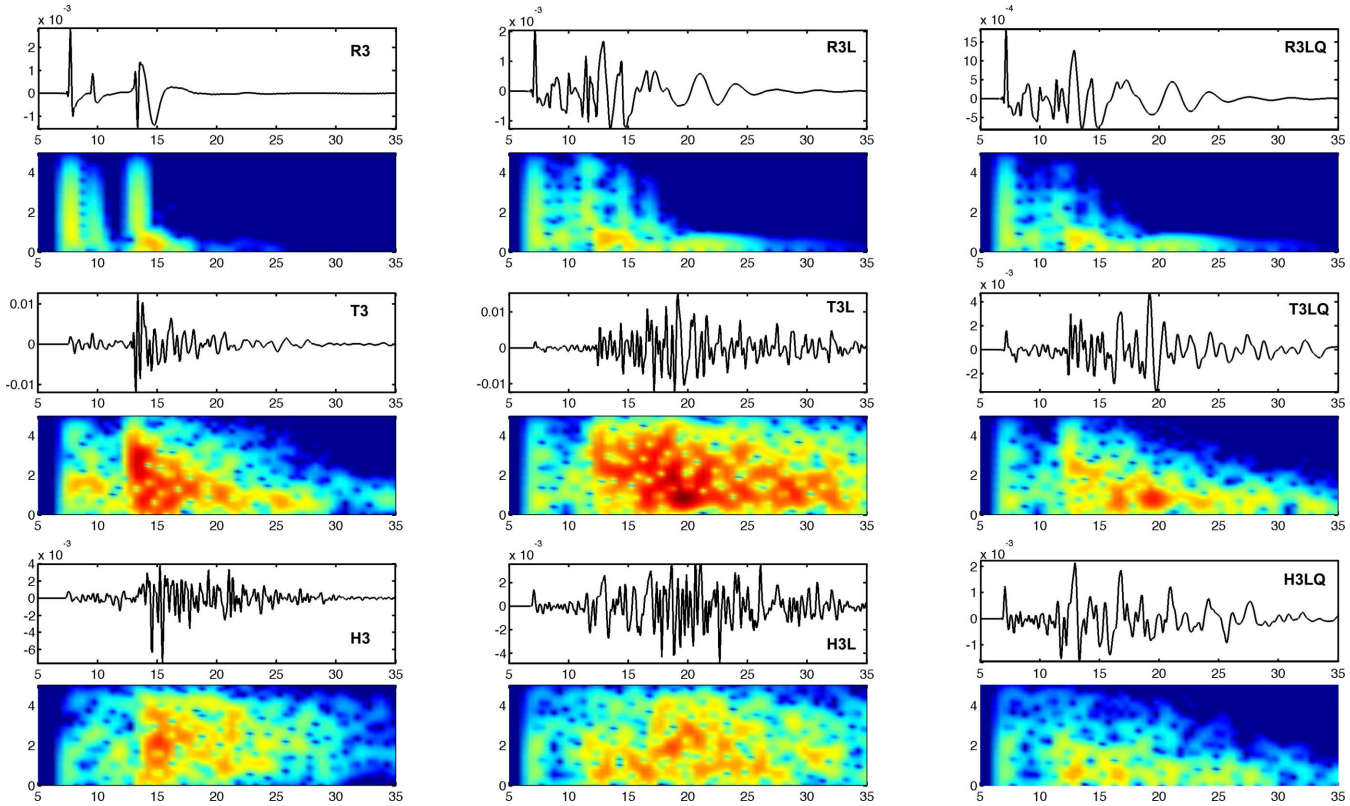

Figure 5. Velocity time-series (vertical component) and spectrograms (time-frequency analysis) of a receiver located at ($x = 40$ km, $y = 40$ km) for source S1. Only a subset of models is shown (see labels). Waveform amplitude units are m s^{-1}, while horizontal (time) axis units are seconds. All spectrograms have identical colour scale. Spectrograms reveal the different spectral content of coda waves for topography and heterogeneity scattering. Intrinsic attenuation produces similar effects on both cases.

by velocity heterogeneity in a narrow (2–3 s long) time-window starting immediately after the average direct *S*-wave arrival time, marked by a vertical dashed line. We observe that this holds to some extent also for more realistic velocity models including near-surface low-velocity layer and intrinsic attenuation (Fig. 7, left column). However, as time increases such difference vanishes quickly and coda become fairly comparable also at large time lapses (see insets in Fig. 6, left column). An exception here is represented by model T2S3, showing smaller late coda due to the mild topographic profile in the upper-left area of model T2.

For constant background velocity and at larger distance from the source (Fig. 6, right column), we observe a similar pattern although velocity heterogeneity may excite coda waves more efficiently in a time-window roughly comprised between the envelope peak and two times the direct *S*-wave arrival. Despite the limited source–receiver separation in our study, velocity perturbations already introduce a lag between the *S*-wave onset and the envelope peak, a characteristic widely observed in actual ground-motion recordings, especially at regional and teleseismic distances (Sato & Fehler 1998). Topography only does not reproduce this observation, because direct waves travel undisturbed in the medium until they impinge the corrugated free-surface: as a result, envelopes appear highly asymmetric. However Fig. 7 suggests that topography can excite larger late coda ($t > 2T_S$) when these are mainly composed by surface waves, regardless of the distance from the seismic source. In this case, velocity heterogeneity affects mainly the interval between the *P*-wave and the surface wave onset, thus indicating a more efficient scattering of body waves. Figs 6 and 7 also illustrate that both topography and velocity heterogeneity are responsible for envelope broadening, that is, the apparent duration of envelopes increases with the propagation distance.

A straightforward measurement of scattering is represented by the coda-Q coefficient Q_c, as introduced in the single scattering model of Aki & Chouet (1975). This model assumes that scattering is weak and therefore multiple scattering can be ignored. The coda of local earthquakes is formed by waves that travel outward from the source, are back-scattered by heterogeneities in the lithosphere, and then propagate back to the receiver. The waves are attenuated along the paths from the source to the scatterer and from the scatterer to the receiver. The single-scattering model does not separate intrinsic and scattering attenuation, but instead combines them into a single term, Q_c, that is used to quantify the coda decay rate through the following exponential form:

$$A(f, t) = A_0(f)t^{-n}\exp(-\pi f t/Q_c) \tag{3}$$

where f is frequency, $A_0(f)$ is the coda source factor, t is the lapse time, and t^{-n} is the geometrical spreading function, where n can be equal to 0.5, 0.75 or 1 depending on the dominance of surface, diffusive or body waves (Sato & Fehler 1998). Eq. (3) is valid for lapse times greater than twice the direct *S*-wave traveltime (Rautian & Aki 1978) and therefore we use it to evaluate only the late coda.

In the framework of our study, we relax the simplistic assumptions of the single backscattering as we are primarily interested in a relative comparison between coda waves. We set n equal to 1 for consistency with available attenuation studies, despite the presence of important surface waves in some of our models. Q_c is then estimated by fitting the root-mean-square envelopes to eq. (3) within a 20-s-long time-window starting at twice the *S*-wave arrival time

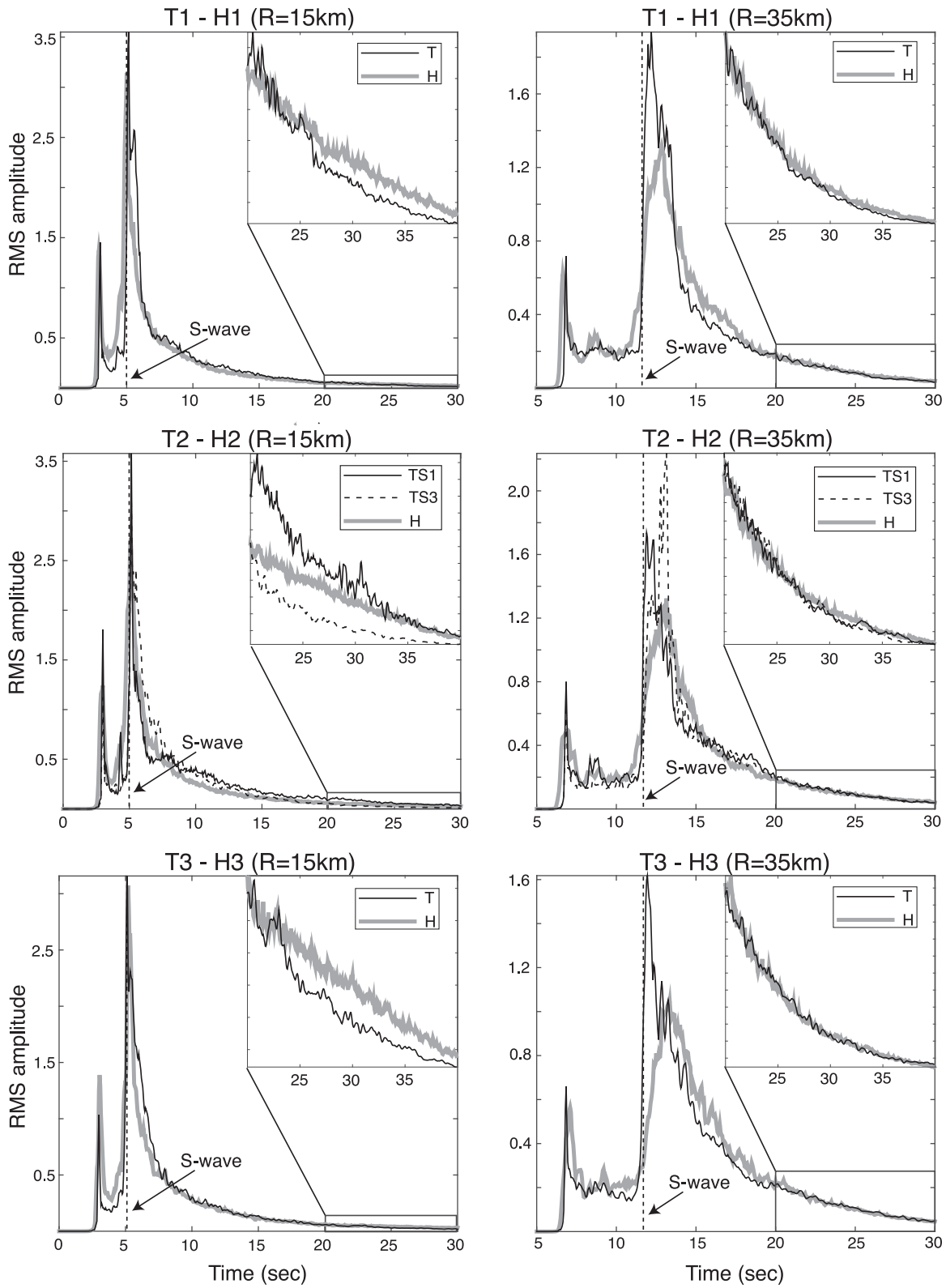

Figure 6. Velocity vertical component normalized RMS envelope $\bar{E}_{\mathrm{rms}}(t)$ for models T1, T2, T3, H1, H2 and H3. Results are averaged over source realizations S1 and S3. Two sets of envelopes at hypocentral distances of 15 and 35 km are shown. For model T2, contributions of sources S1 and S3 are displayed separately due to the strong asymmetry of the topography. Insets show envelopes in the 20–40 s time-window. Dashed vertical line indicates the mean direct *S*-wave arrival time computed by averaging over all receivers. Vertical scale is different for each panel. RMS envelopes are comparable at large time lapses for both sets of models.

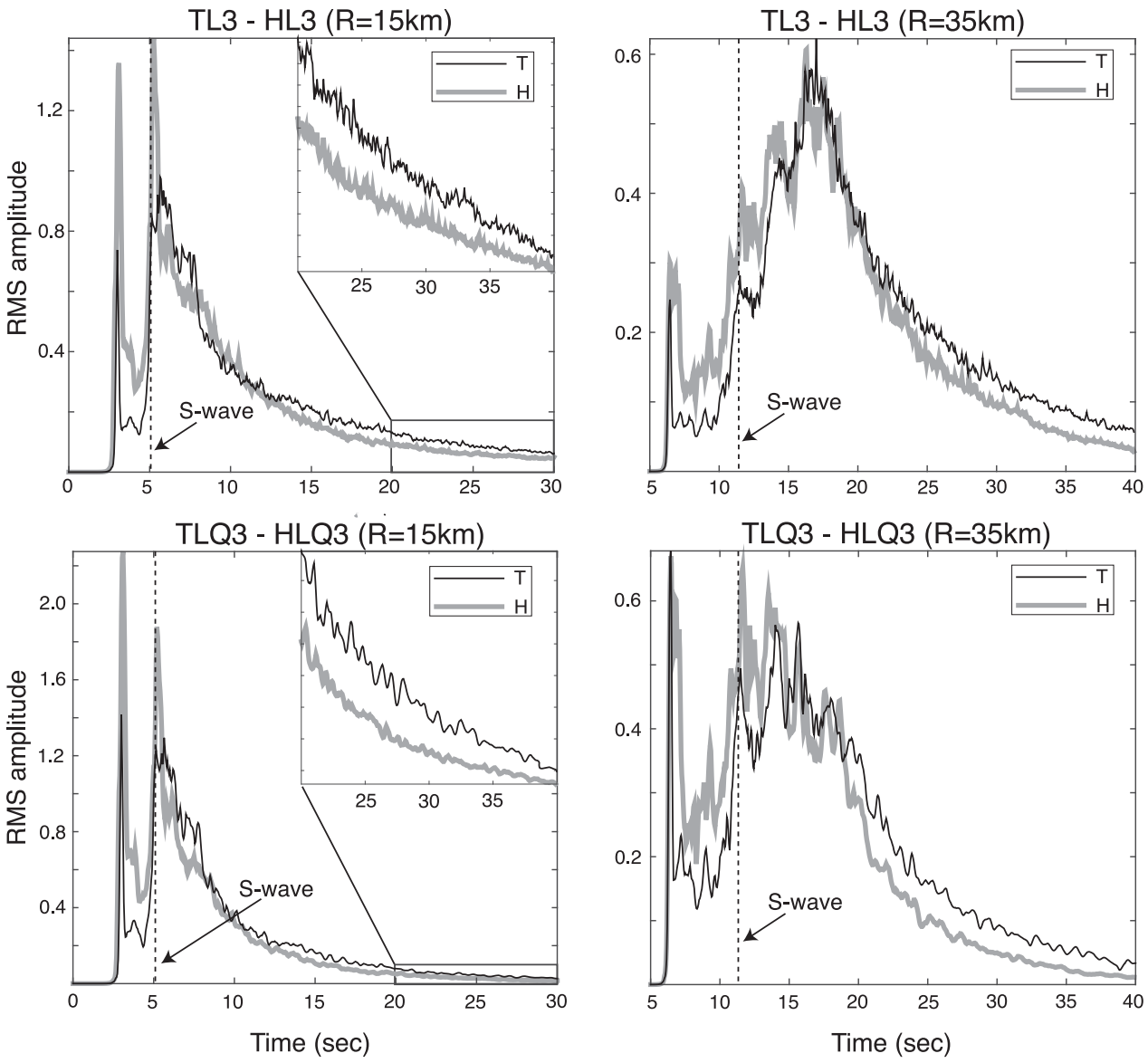

Figure 7. Same as Fig. 6, but for models T3L, T3LQ, H3L and H3LQ. Results are averaged over source realizations S1 and S3. Two sets of envelopes at hypocentral distances of 15 and 35 km are shown. Insets in the left column show envelopes in the 20–40 s time-window. Dashed vertical line indicates the mean direct *S*-wave arrival time computed by averaging over all receivers. Vertical scale is different for each panel. Note that RMS envelope $\bar{E}_{\mathrm{rms}}(t)$ is larger for models with topography at late coda ($t > 2T_s$).

at receivers 25 km away from sources S1 and S3, located approximately in the centre of our models. We consider three frequency bands (0.75 ± 0.25, 1.5 ± 0.5 and 3.0 ± 1.0 Hz) typically used in attenuation studies. Results are summarized in Table 2, showing that the difference between the late coda generated by topography and velocity heterogeneity is frequency-dependent and negligible at low frequency, while at high-frequency velocity heterogeneity scatters energy more efficiently than topography. However, this difference vanishes when the wave field is dominated by surface waves and both mechanisms result in comparable coda decay rates. The introduction of intrinsic attenuation increases the decay rate especially in presence of topography, as scattering occurs only at the free surface where the highest anelastic absorption is found.

Direct comparisons of our results with Q_c values inferred for the Earth crust are limited by a number of factors, for example the use of a single time lapse in this study, compared to several time-windows applied to observational data, and the lack of intrinsic attenuation for a large group of our models. Measured coda Q is often found either close to the intrinsic attenuation as predicted by theory (e.g. Frankel & Wennerberg 1987) or to the total attenuation (e.g. Mayeda *et al.* 1992; Bianco *et al.* 2005).

Although most of our numerical models are purely elastic (i.e. $Q_i^{-1} \gg 1000$), it would be incorrect to compare Q_c with the scattering attenuation Q_s, whose measurements can be obtained through the MLTW technique (Hoshiba 1993), as pointed out by Hoshiba (1991) and Wennerberg (1993). However, for models TLQ3 and HLQ3 a direct comparison with available Q_c values is possible, revealing lower than expected values already at 1.5 Hz, and even more so at 3 Hz. Measurements of Q_c made for different tectonic settings throughout the world show variations from region to region larger than a factor of 10 (Sato & Fehler 1998). In general, Q_c values in the range 50–100 at 1.5 Hz, and 150–200 at 3 Hz have been reported (e.g. Mayeda *et al.* 1992; Akinci & Eyidoğan 2000; Tuvé *et al.* 2006, among the others).

Table 2. Coda quality coefficient Q_c at hypocentral distance of 25 km and three frequency bands. Values are obtained by fitting the filtered root-mean-square envelopes to eq. (3). We consider a single 20-s-long time-window starting at twice the *S*-wave arrival time.

	Qc		
Models	0.75 Hz	1.5 Hz	3.0 Hz
T1	20.5	38.4	63.7
T2	21.8	36.9	62.9
T3	29.6	41.3	63.7
H1	26.0	47.9	99.2
H2	25.9	50.5	106
H3	25.1	53.3	108.9
TL3	68.2	110	188.4
TLQ3	31.8	42.2	59.5
HL3	34.4	73.3	150.4
HLQ3	21.8	36.9	59.3

The origin of this discrepancy is threefold: coda attenuation is known to present a time-lapse dependency, probably related to inhomogeneous distribution of scatterers and depth-dependent intrinsic attenuation in the crust (e.g. Hoshiba 1994). In this study, we are obliged to evaluate Q_c at a time lapse smaller than in many attenuation studies and, as shown in Tuvé *et al.* (2006), this could lead to lower values. On the other hand, the shallow depth at which we deployed the point-source forces the seismic waves to propagate prevalently in the shallow low-velocity layer characterized by very high attenuation values, while databases used in attenuation studies usually comprise deeper events able to sample regions of the crust where attenuation is weaker (Bethmann *et al.* 2012). As a result, our estimates are closer to those for the shallow crust (e.g. Kosuga 1992). At the same time, intrinsic attenuation is modelled as almost constant over the whole frequency range in our numerical simulations, although it is often reported to decrease rapidly with frequency already above 1 Hz. Therefore, we may overestimate the effects of intrinsic attenuation in the high-frequency range.

The $\bar{E}_{\mathrm{rms}}(t)$ analysis presented in Figs 6 and 7 does not consider any potential space-variability of the coda envelopes associated to the topography and velocity heterogeneity distribution. We therefore introduce the total coda energy E_c at each receiver:

$$E_c = \frac{\sum_{i=x,y,z} \int_{t_0}^{t_{\max}} v_i(t)^2 \, \mathrm{d}t}{\sum_{i=x,y,z} \int_{0}^{t_{\max}} v_i(t)^2 \, \mathrm{d}t}, \tag{4}$$

which quantifies the energy content of coda waves. We set t_0 equal to the direct *S*-wave arrival time plus 3 s to minimize the effect of the ballistic wave in the calculations. In Fig. 8, we show maps of the coda energy ratio derived by subtracting the coda energy of the velocity heterogeneity model (H) from the coda energy of the corresponding model with topography (T), dividing the result by the coda energy for the first model and multiplying the result by 100. A particularly interesting case is represented by model T2, where results are strictly

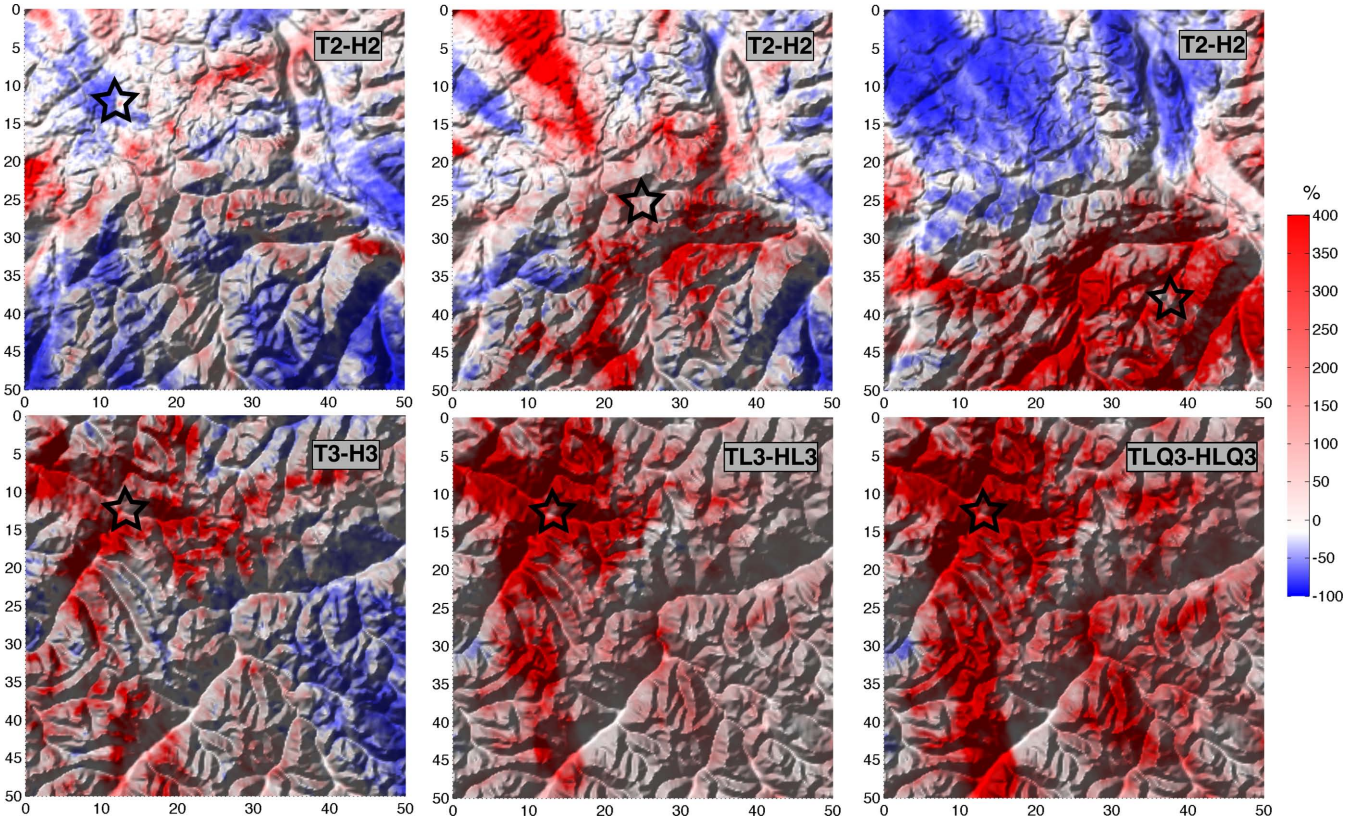

Figure 8. Coda energy ratios for some of the models used in this study. Black star indicates source position. The coda energy (E_c) is computed according to eq. (4) using all components of motion. Each ratio is then derived by subtracting the coda energy for the flat model (H) from the coda energy for the corresponding model with topography (T), dividing the result by the coda energy for the flat model and multiplying the result by 100. Results denote large spatial variability of the coda wave energy content, depending also on source position.

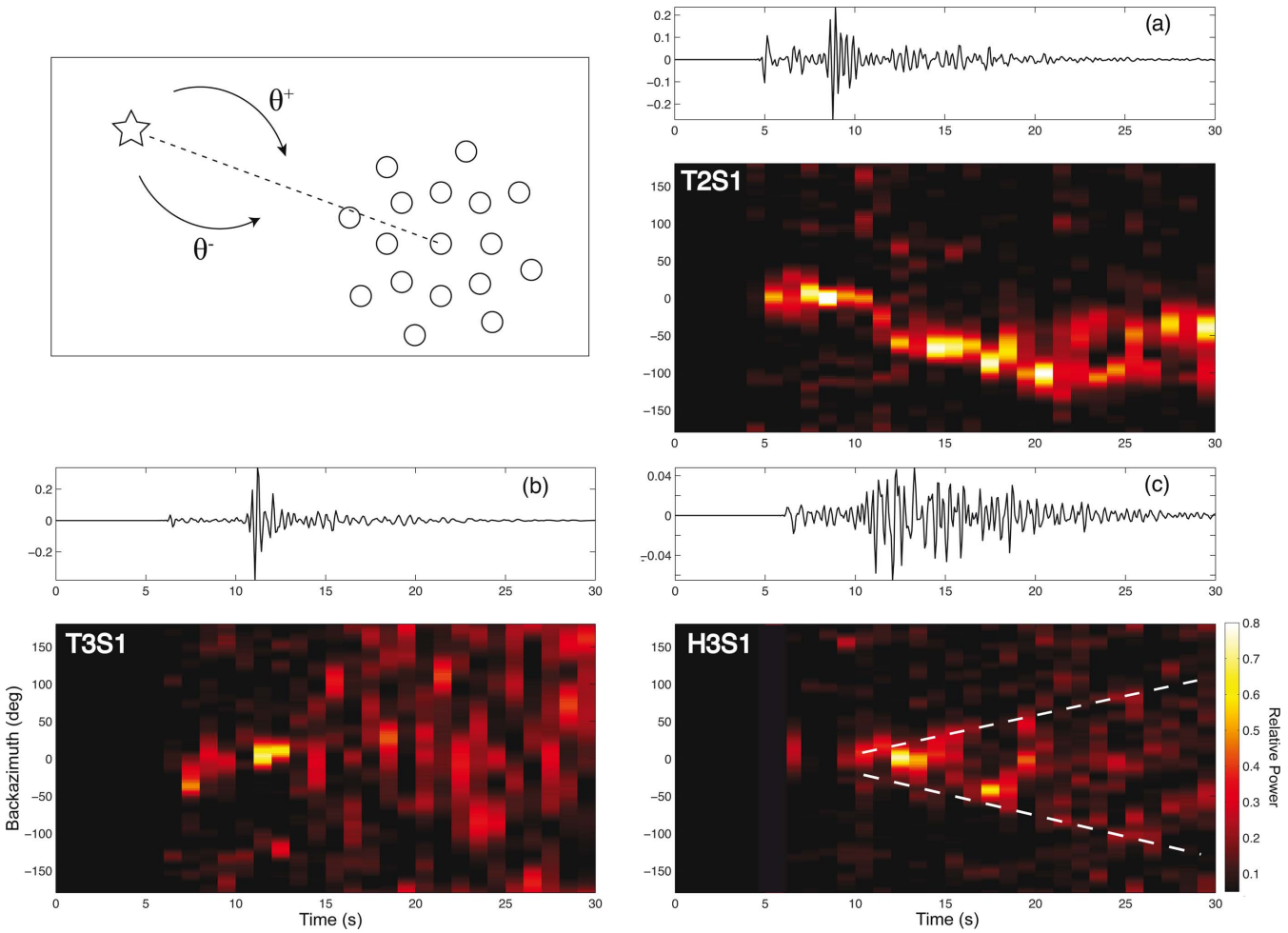

Figure 9. Vespagrams computed from acceleration time-series (vertical component) observed at a 3-km aperture array located at ($x = 34$ km, $y = 36.2$ km) for models (b) T3S1 and (c) H3S1. For model T2S1 (a) the array is located at ($x = 37$ km, $y = 8.4$ km)—see also Fig. 1. Plots show the beam energy at a constant apparent velocity of 3 km s^{-1} and different back azimuths. Time-series on top of each panel are recorded at the array centre. The relative power is a measure of signal coherence across the array. Each vespagram is computed using a 1-s-long sliding window moved forward in 1-s steps. The two dashed lines in panel (c) indicate how the back azimuth increases with time. The colour scale has been partially clipped for better visualization.

dependent on the source position as a consequence of the irregularity of the topographic surface. In general, we find that topography constitutes the principal scattering mechanism in proximity of the epicentre for most of the models, but its contribution can be locally significant even at larger distances, depending on the characteristics of the free surface. This is not surprising since the strongest scattered waves emanate from locations of strong topographic gradients, as previously documented by numerical experiments (e.g. Pitarka & Irikura 1996; Hestholm *et al.* 1999; Ripperger *et al.* 2003). Fig. 8 indicates also that intrinsic attenuation has a smaller effect in case of topography scattering, probably due to the long-period surface waves composing most of the coda wave train.

4.2 Array analysis

Directionality effects of the scattering process can be investigated more in detail using the vespagram analysis (Davies *et al.* 1971; Rost & Thomas 2002), which calculates the power distributed among different directions of incidence (back azimuth, θ) and a specific apparent slownesses (u), or vice versa, by stacking seismic records at different reduced times depending on the relative location of the station. The resulting beam energy is then plotted along the time axis.

Here we consider an array formed by 17 receivers arranged in two concentrical circles, with radii of 750 and 1500 m, respectively (Fig. 9; see Fig. 1 for the location of the arrays). These array dimensions allow us to treat travelling wave fronts as plane waves across the array without sacrificing back azimuth and slowness resolution. As we are primarily interested in determining the arrival direction of the seismic energy at the array, we consider only the vertical component of motion and use a 1.0-s-long sliding-window shifted along the seismogram. Fig. 9 depicts conceptually the back azimuth angle as well as results for three different models at a constant apparent velocity of 3 km s^{-1}. We find that most of the energy crosses the array at this specific apparent speed for the considered epicentral distances, with the exception of *P* waves in the early part of time-series.

First, we consider model T2, where the asymmetry characterizing topography is well reflected in the vespagram: for the selected array location, the arrival direction of most of the coda energy is comprised within a narrow back azimuth range (Fig. 9a), indicating that waves are scattered by prominent topographic features located southwards of the array. High values of relative power indicate also

that these waves cross the array coherently, thus confirming they originate from distant irregularities at the free surface. However, when the array is surrounded by regular topography, as in model T3, we observe scattered waves crossing the array from different directions, even opposite respect to the direct-wave travel path (Fig. 9b).

On the other hand, the effects of random velocity perturbations are dramatically different, as shown for model H3 in Fig. 9(c). While for model T3 some coherency is preserved even at large time lapses, coda waves crossing the array now appear to be incoherent already a few seconds after the *S*-wave arrival. Interestingly, this is in agreement with the observations of Dominguez *et al.* (2013), who found a significant drop in coherency as coda waves built up for two local events at Long Beach, California.

We note also that the back azimuth angles of incoming waves for model H3 are more clustered around the direct-wave travel direction. The two dashed lines in Fig. 9(c) indicate how the back azimuth increases with time, thus suggesting a possible transition from forward- to back-scattering, in agreement with the model proposed by Sato *et al.* (2004).

4.3 Radiation pattern

Recently, numerical simulations based on 2-D and 3-D models (Takemura *et al.* 2009; Imperatori & Mai 2013) have demonstrated that small-scale velocity heterogeneities in the crust are able to effectively destroy the apparent *S*-wave radiation pattern as a consequence of seismic wave scattering (e.g. Aki & Chouet 1975). Alternatively, mixing and coupling of SH and SV waves was suggested as a mechanism for the frequency-dependent radiation pattern distortion (Takenaka *et al.* 2003). Out-of-plane effects are particularly important in presence of rough topography, and phase conversion can be widely observed (e.g. Hestholm *et al.* 1999; Rodgers *et al.* 2010).

We therefore compare the effects of topography and velocity heterogeneity on the radiation pattern in three distinct frequency bands, 1.0 ± 0.5, 2.5 ± 0.5 and 4.0 ± 0.5 Hz. Following Takemura *et al.* (2009), we consider the rms quantity $A_T = \frac{T}{\sqrt{T^2+R^2}}$, where R and T are the absolute maximum amplitudes of the S wave in radial and transversal motions, respectively. Maximum values are extracted for receivers between 20 and 25 km from the epicentre in a 5-s-long time-window starting at the direct *S*-wave arrival time. Time-series are converted to acceleration and then filtered using a four-pole bandpass Butterworth filter prior to calculations.

Results for several models are shown in Fig. 10, along with the theoretical A_T value (dashed line). For those models featuring a low-velocity layer, this is replaced by average A_T values found for the corresponding reference model. We note that both velocity heterogeneity and topography contribute to the radiation pattern distortion, which increases with frequency. The effect of topography, however, is generally weaker and strictly correlated to the roughness of the free surface, as can be seen in the almost unaltered radiation pattern in the northern quadrants for model T2. It is interesting to note that the distortion induced by a highly irregular topography, as in model T3, produces effects comparable to velocity perturbations except in proximity of the nodal axis, where the radiation pattern is less affected.

Our analysis also reveals that topography results in overall lower and more variable A_T values, indicating a more efficient mode coupling compared to the velocity heterogeneity case due to of the higher reflection coefficient at the free surface. Intrinsic attenuation tends to reduce the radiation pattern distortion, most notably in the models with topography, in which energy is scattered exclusively at the free surface.

A more quantitative comparison with available observations (Takemura *et al.* 2009) is restricted mainly by the short epicentral distance range and the limited frequency bandwidth of our simulations. However, qualitatively, we notice that our synthetic data generally agree with observations, except for somewhat larger A_T values at high-frequency. This discrepancy could originate from non-pure strike slip mechanisms and non-dc source components in the aftershock sequence analysed by Takemura *et al.* (2009).

4.4 Ground-motion variability

The analysis of well-recorded earthquakes reveals a large variability of ground-motion intensity measures such as PGA or PGV in the near field (e.g. Shakal *et al.* 2006). This variability may originate from differences in local site conditions, from wave propagation effects such as scattering of seismic waves, and from complexities of the rupture process. The latter is thought to be significant, particularly in proximity of the fault (e.g. Guatteri *et al.* 2003). On the other hand, scattering is generally thought to play an important role at large distances (Spudich & Chiou 2008).

However, Imperatori & Mai (2013) have shown that small-scale velocity heterogeneity can be responsible of significant ground-motion variability even at short distances from the fault. This complexity is reflected not only in the variability of scalar intensity measurements (PGA, PGV), but also in the drop of time-series coherence between neighbouring stations. Strong velocity perturbations may even blur significantly the wavefield signature of Mach wave fronts (Imperatori & Mai 2013).

In Figs 11 and 12 we show how velocity heterogeneities and topography affect PGV at 10 and 30 km from the source for our models with constant and variable background velocity, respectively. For each station, we define the residual as $\ln(\frac{\mathrm{PGV}}{\mathrm{PGV_{ref}}})$, where $\mathrm{PGV_{ref}}$ is the PGV value from the corresponding reference model. We consider the geometric mean of peak motions in the horizontal plane and neglect those receivers within 5° from the nodal planes to minimize the influence of values biased by radiation pattern effects. Additionally, in Table 3 we report the mean (μ) and the intraevent standard deviation (σ) of the residuals shown in Fig. 11. The latter expresses the variability for a single simulation considering all receivers at the same distance. The standard deviation value reported in Table 3 is averaged over all three source realizations.

Results indicate that random velocity perturbations generate overall larger ground-motion variability than topography. Although the average standard deviation is almost identical at close distance from the source, it is roughly doubled at 30 km. We observe that the same holds for those models featuring a shallow low-velocity layer. It is worth noticing that intrinsic attenuation decreases the ground-motion variability of about 0.06 units of standard deviation in average, as a result of the dramatic amplitude drop of coda waves (Fig. 4). Similarly, continuous scattering through the volume results in larger apparent attenuation, indicated by lower mean values of residuals for those models containing velocity heterogeneity. Such behaviour is not surprising, as synthetics of models with topography have larger peak amplitudes due to shear waves (Fig. 3) and surface waves (Fig. 4).

Although smaller, the variability induced by topography is not negligible. By comparison, standard deviation from empirical ground-motion prediction equations at 30 km on rock soils

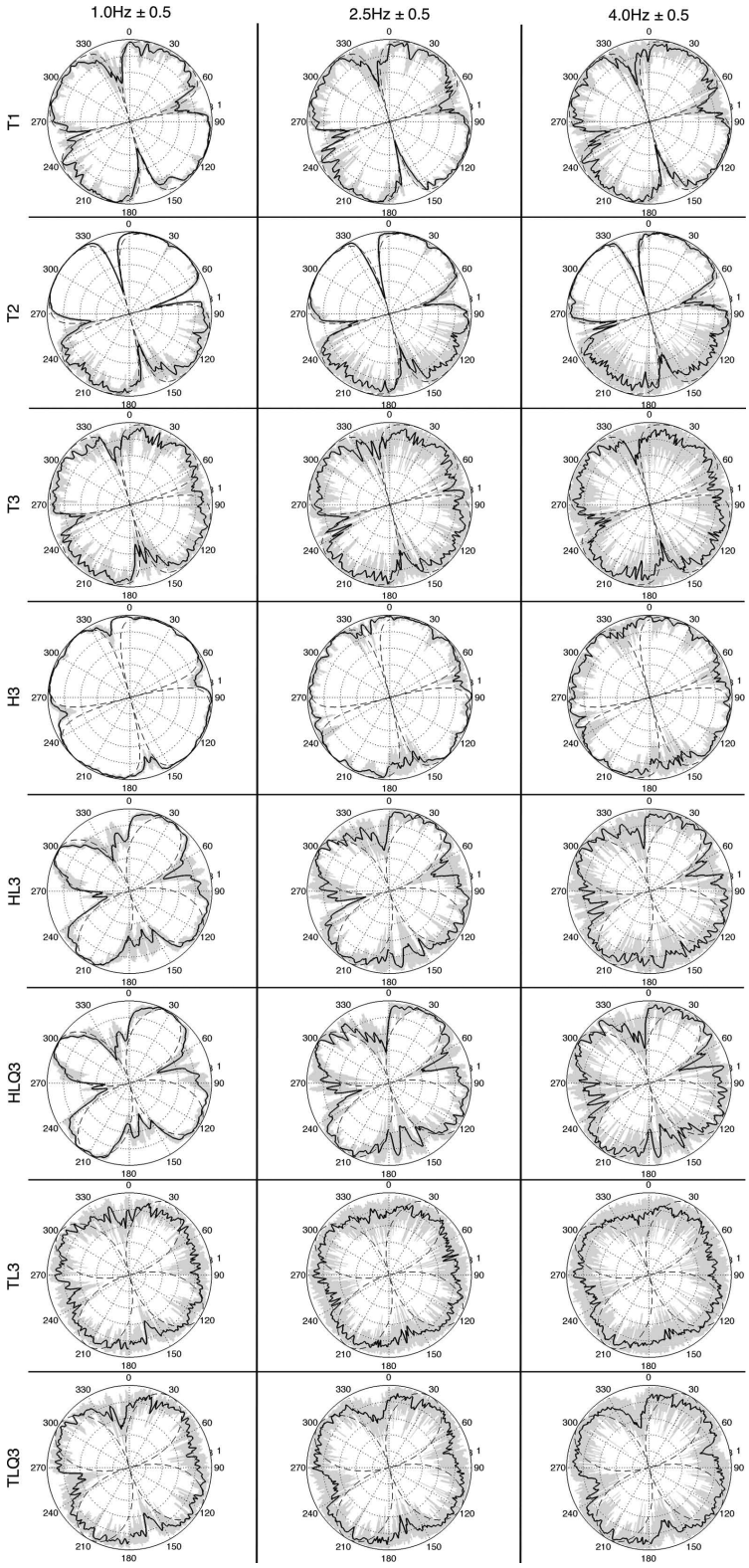

Figure 10. Maximum *S*-wave amplitude in transverse motion A_T as a function of azimuth at three different frequency bands. Grey-shaded areas indicate all values, while the continuous black line represents values averaged over a 1-deg-wide azimuth window. For models T1, T2, T3 and H3 the dashed line represents theoretical A_T values, while for the remaining models it is based on A_T values as computed from the corresponding reference model.

($V_{S30} = 760\,\mathrm{m\,s^{-1}}$) is about 0.6 in the 1–10 Hz frequency range (Abrahamson *et al.* 2008). It is therefore important to consider the combined effect on ground-motion variability of both topography and velocity heterogeneity. For this purpose, we compute synthetics for a new model obtained by blending models T3 and H3. Model T3 represents an interesting case because it is characterized by larger sigma than other topography models. We neglect low-velocity layers and intrinsic attenuation to limit the computational cost. Moreover,

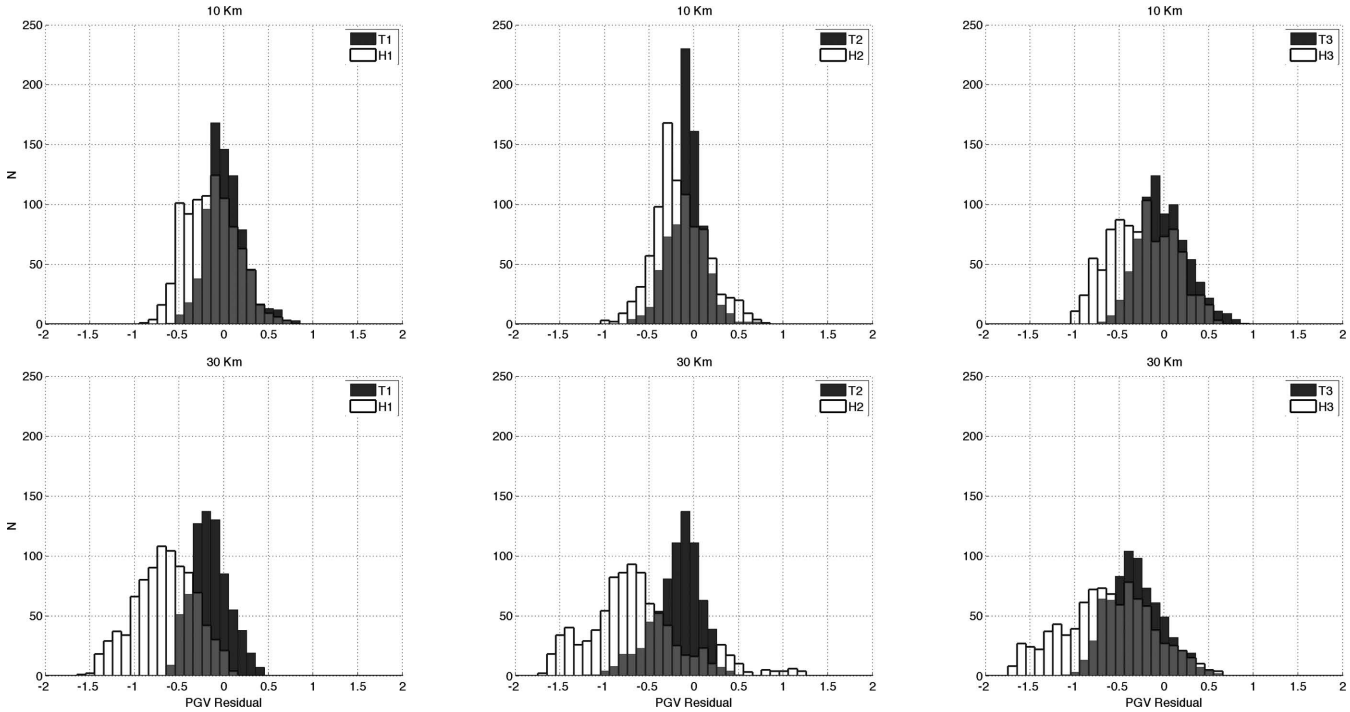

Figure 11. Distribution of residuals ln (PGV/PGV$_{ref}$) of horizontal PGV (geometric mean) at 10 and 30 km distance range for all the homogenous background velocity models. PGV$_{ref}$ is referred to the corresponding reference model (R). Mean and standard deviation are reported separately in Table 3. Note that each white histogram is partially transparent to let the back-standing dark grey histogram be fully visible.

as shown in Table 3, they have only a second order effect on PGV variability. For the new model, we obtain average intraevent standard deviation values of 0.41 and 0.56 at 10 and 30 km, respectively. These values are higher than those obtained for models T3 and H3 separately, especially at very short distance. This indicates that the combined effect of rough topography and velocity heterogeneity further increases ground-motion complexity at all distances.

5 DISCUSSION AND CONCLUSIONS

We have carried out numerical experiments to understand differences and similarities between the scattering due to topography and velocity heterogeneity. One of our goals was to examine whether topography could be used as a proxy for heterogeneity scattering, which, if true, would facilitate realistic 3-D ground-motion simulations for engineering purposes. We have focused our attention on the near-source region ($R < 50$ km), where the strongest ground motion is observed and relatively few observations are available. Limiting the extension of the numerical models, and therefore their computational costs, allowed us to simulate ground motion up to 5 Hz including realistic features as low-velocity velocity layers and intrinsic attenuation. We deployed a point source characterized by an ω^2 spectrum, with corner frequency around 1 Hz, as we are interested in wave propagation effects only. Random velocity heterogeneity distributions are modelled using Von Karman autocorrelation functions, whose parameters are based on previous studies (e.g. Imperatori & Mai 2013; Takemura & Furumura 2013).

We consider three topography models of the Swiss alpine region with different degrees of roughness and height distribution characteristics, making them representative of many other mountain regions around the world. In this study we do not include sedimentary basins, which are known to greatly influence wave propagation (e.g. Stupazzini *et al.* 2009), as we are primarily interested on the effects of the random, small-scale lateral velocity variations.

Our simulations reveal that the two scattering mechanisms are intrinsically different, and result in different wavefield characteristics. In particular, from the analysis of root-mean-squared envelopes in homogenous background velocity media, we observe that topography produces asymmetric ground-motion envelopes at all epicentral distances considered, with amplitude peaks corresponding to the direct *S* wave and then exponentially decaying to lower amplitude levels. On the contrary, velocity heterogeneity scattering results in envelopes where the lag between *S*-wave onset and peak increases with epicentral distance (Fig. 6). This feature is normally observed in recorded seismograms worldwide (Sato & Fehler 1998). Taking into account these differences alone, we conclude that topography scattering cannot be used as an approximation to velocity heterogeneity scattering.

In Fig. 13, we show conceptual waveform envelopes according to the multiple *S*-to-*S* scattering model of Zeng (1991, 1993) and the Markov approximation of the parabolic wave equation (e.g. Sato 1989; Sato & Fehler 2007). The first model, based on the radiative transfer theory, provides the temporal energy decay of multiply isotropic backscattered waves in a uniform random medium. The second model accurately describes diffraction and scattering around the forward direction. The Zeng's model is also applied in the hybrid broadband synthetics technique of Mai *et al.* (2010).

Interestingly, comparisons between Figs 13 and 6 suggest that topography scattering can be reasonably approximated by backscattering models. On the other hand, forward-scattering models better predict velocity heterogeneity scattering, at least in the early coda section. Our conclusion is supported by the analysis of arrival directions at small-aperture arrays, indicating that coda waves generated by topography scattering are mainly composed by backscattered waves, including long period surface waves.

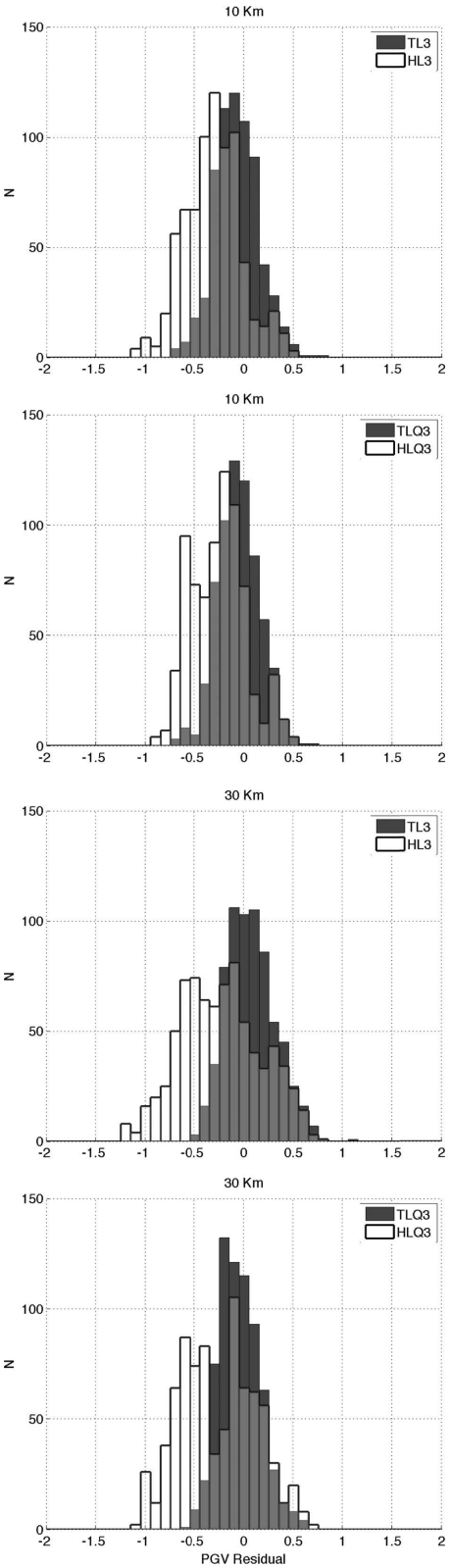

Figure 12. Same as for Fig. 11, but for models T3L, H3L, T3LQ and H3LQ. PGV_{ref} is referred to the corresponding reference model (RL and RLQ). Mean and standard deviation are reported separately in Table 3. Note that each white histogram is partially transparent to let the back-standing dark grey histogram be fully visible.

Table 3. Mean (μ) and intraevent standard deviation (σ) of residuals shown in Fig. 10. σ is calculated separately for each simulation over receivers at a given distance, and then its mean value is returned.

	10 Km		30 Km	
Models	μ	σ	μ	σ
T1	0.01	0.21	–0.16	0.21
T2	–0.08	0.18	–0.19	0.24
T3	–0.01	0.27	–0.32	0.29
H1	–0.15	0.28	–0.67	0.32
H2	–0.16	0.27	–0.64	0.50
H3	–0.26	0.29	–0.63	0.47
TL3	–0.07	0.25	0.07	0.29
TLQ3	–0.06	0.23	–0.05	0.22
HL3	–0.31	0.28	–0.24	0.49
HLQ3	–0.26	0.25	–0.26	0.38

Velocity heterogeneity scattering produces incoherent body-wave energy scattered predominantly in the forward direction. At larger time lapse, however, an increase in the back-scattered energy component would indicate that hybrid models, as the one proposed by Sato *et al.* (2004), combining forward- and back-scattering, may effectively explain wave envelopes from onset to late coda in random media having rich short wavelength spectra.

We also find that our simulations are in good agreement with the empirical observations of Wagner (1997) for regional wave propagation in southern California and Nevada, who suggested that *P*- and *S*-wave trains are composed by forward scattered energy and that scattering sources are located in a limited volume subparallel to the path of the direct arrivals. Wagner (1997) also found that only surface waves exhibit a character consistent with the random scattering model for coda generation.

The differences between scattering due to topography and velocity heterogeneity illustrated so far can be explained considering the different scattering mechanism at the base of the two set of models. Multiple scattering caused by small-scale velocity perturbations, occurring continuously in the whole volume, leads to more gentle coda decay and to envelope broadening. On the other hand, if only topography is present, the wave field propagates undisturbed until it impinges the corrugated free surface, where large impedance contrasts lead to well-developed early coda immediately after the direct wave. At the same time, this mechanism can result in strong reflected and diffracted phases by prominent topographic features and also in more efficient mode mixing, as shown in our radiation pattern analysis.

Our simulations also reveal that topography and velocity heterogeneity scattering can produce comparable coda-wave energy, mainly around 1 Hz, although large variability in space should be expected. We find that simply changing the source position translates into relevant increase/decrease of coda waves. Similar results for Northern Taiwan were found by Lee *et al.* (2009), who described a complex interaction between topographic effects and source location. Eventually, topography scattering can be the dominant process, especially if the seismic source excites surface waves. Analogous conclusions were reported in O'Brien & Bean (2009), who compared the effects of volcano topography and internal heterogeneous volcanic structure and found that topography acts as the principal scatterer. Recently, Magnoni *et al.* (2014) analysed the wave field generated by the M_w 6.3 L'Aquila earthquake, remarking that the

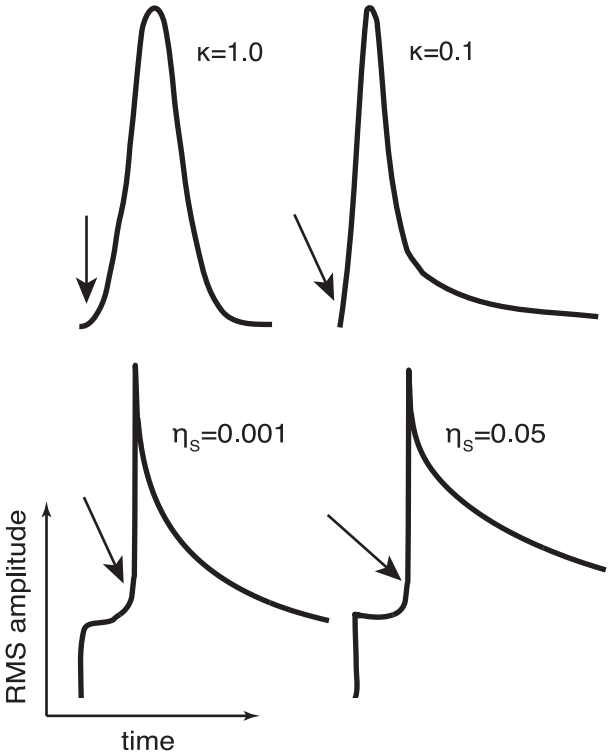

Figure 13. Top: typical RMS Markov envelopes from an explosive source in Von Karman random media with different spectral decay controlled by Hurst exponent κ equal to 1.0 and 0.1 (modified after Sato & Fehler 2007). Arrows mark *P*-wave first arrival time. Bottom: RMS envelopes produced by a double-couple point-source in a medium with uniform scatterers distribution according to the multiple *S*-to-*S* scattering model of Zeng (1991, 1993) for two different scattering coefficients (modified after Imperatori & Mai 2013). Arrows mark direct *S*-wave arrival time. Markov envelopes are dominated by forward scattering, while Zeng's envelopes are determined by backscattering. Note that the envelopes are conceptual and not aligned in time.

sole introduction of topography in their models improved the fit between synthetics and observed seismograms in the coda part of the signal.

The presence of near-surface low-velocity layers has a dramatic effect on the simulated ground motion. We find that shallow sources can generate large amplitude surface waves scattered by both topography and velocity heterogeneity that dominate synthetics in a wide distance range. Resulting time-series envelopes show a time-dependent lag between the *S*-wave onset and the envelope peak, corresponding to the surface wave train.

Imperatori & Mai (2013) recently reported that low-velocity layers increase coda wave amplitude and duration by trapping energy close to the free surface. Our results confirm the importance of shallow subsurface structures for waveform complexity, as also pointed out by Spudich & Bostwick (1987) and Dodge & Beroza (1997), who found evidence for near-surface scattering in Southern California. Similarly, Vernon *et al.* (1998) observed frequency-dependent scattering occurring in the weathered layer underneath the Pinyon Flats array.

As most of the scattering occurs in proximity of the free surface, wave propagation simulations at intermediate frequency require intrinsic attenuation Q_i^{-1} to be taken into account. In our approach, we model absorption as constant over the whole 0–5 Hz frequency band. This may lead to overestimated attenuation towards the upper end of the spectrum, since Q_i^{-1} is expected to decrease with frequency above 1 Hz (e.g. Sato & Fehler 1998). Although a more realistic representation of intrinsic attenuation is highly desirable, given the limited frequency band of our simulations, we consider our findings robust. Similar to O'Brien & Bean (2009), we notice that intrinsic attenuation reduces coda duration but not waveform complexity. As a result, the wavefield for models featuring a low-velocity layer and intrinsic attenuation is more complex than for elastic models with homogenous background velocity.

Complex wave propagation effects influence also the radiation pattern recorded at the surface and the ground-motion variability. Our investigations indicate that rough topography could play an important role in the distortion of the source radiation pattern, a frequency-dependent phenomenon typically attributed to velocity heterogeneities (Takemura *et al.* 2009).

Imperatori & Mai (2013) investigated a large number of random velocity distributions and demonstrated that velocity heterogeneity can induce relevant ground-motion variability already at distances in the range of 10–25 km from the source. At such short distance, the ground shaking was generally thought to be dominated by source rupture complexity (e.g. Ripperger *et al.* 2008). Intraevent standard deviation estimates obtained in this study are in agreement with the work of Imperatori & Mai (2013) and indicate that the PGV variability and the apparent attenuation induced by topography is always lower than those associated with velocity heterogeneity, although the difference reduces sensibly at very short distance (e.g. 10 km).

However, we note that PGV variability values derived from combining topography and velocity perturbations are comparable with those derived from dynamic rupture simulations in the near-source region as obtained by Ripperger *et al.* (2008) and from empirical ground-motion prediction equations (e.g. Abrahamson *et al.* 2008). This further confirms the importance of modelling complex wave propagation phenomena such as scattering in the near source region even at intermediate frequency. We therefore advocate the inclusion of both topography and velocity heterogeneity in earthquake scenario simulations to fully explore the possible range of ground motion.

The seismic source used in the present study is simple but sufficient to isolate and study wave propagation phenomena. However, to further investigate the complex interaction between source and surrounding medium and to compare resulting wavefields with observational data, the introduction of finite-fault ruptures with realistic high-frequency radiation (e.g. Dunham *et al.* 2011) is mandatory. This additional complexity and detail in the modelling setup and data analysis is beyond the scope of this study, but will be presented in a forthcoming paper focused on the ground-motion modelling of the well-recorded M_w 6.6 Western Tottori earthquake.

ACKNOWLEDGEMENTS

We are grateful for the comments from Editor Xiaofei Chen and two anonymous reviewers. Numerical simulations were run on the BlueGene-P 'Shaheen' of the KAUST Supercomputing Lab. We thank A. Petersson for assistance with the WPP code. Research reported in this publication was supported by the King Abdullah University of Science and Technology (KAUST) and partly through a contract with Swiss Nuclear Safety Inspectorate (ENSI).

REFERENCES

Aagaard, B. & Heaton, T., 2004. Near-source ground motions from simulations of sustained intersonic and supersonic fault ruptures, *Bull. seism. Soc. Am.,* **94**(6), 2064–2078.

Abrahamson, N. *et al.*, 2008. Comparisons of the NGA ground-motion relations, *Earthquake Spectra,* **24**(1), 45–66.

Aki, K., 1969. Analysis of seismic coda of local earthquakes as scattered waves, *J. geophys. Res.,* **74**(2), 615–631.

Aki, K. & Chouet, B., 1975. Origin of coda waves: Source, attenuation, and scattering effects, *J. geophys. Res.,* **80**(23), 3322–3342.

Akinci, A. & Eyidoğan, H., 2000. Scattering and anelastic attenuation of seismic energy in the vicinity of North Anatolian fault zone, Eastern Turkey, *Phys. Earth planet. Inter.,* **122**(3), 229–239.

Allmann, B.P. & Shearer, P.M., 2009. Global variations of stress drop for moderate to large earthquakes, *J. geophys. Res.,* **114,** B01310, doi:10.1029/2008JB005821.

Anderson, J.F., Lees, J.M., Waite, G.P. & Johnson, J.B., 2012. Source and propagation effects on near-field co-eruptive ground motion at Santiaguito volcano, Guatemala, *Bull. seism. Soc. Am.,* **102**(2), 696–706.

Assimaki, D., Gazetas, G. & Kausel, E., 2005. Effects of local soil conditions on the topographic aggravation of seismic motion: parametric investigation and recorded field evidence from the 1999 Athens earthquake, *Bull. seism. Soc. Am.,* **95**(3), 1059–1089.

Bethmann, F., Deichmann, N. & Mai, P.M., 2012. Seismic wave attenuation from borehole and surface records in the top 2.5 km beneath the city of basel, Switzerland, *Geophys. J. Int.,* **190,** 1257–1270.

Bianco, F., Pezzo, E.D., Malagnini, L., Luccio, F.D. & Akinci, A., 2005. Separation of depth-dependent intrinsic and scattering seismic attenuation in the northeastern sector of the Italian peninsula, *Geophys. J. Int.,* **161**(1), 130–142.

Bouchon, M., Schultz, C.A. & Toksöz, M.N., 1996. Effect of three-dimensional topography on seismic motion, *J. geophys. Res.,* **101**(B3), 5835–5846.

Brocher, T.A., 2005. Empirical relations between elastic wavespeeds and density in the Earth's crust, *Bull. seism. Soc. Am.,* **95**(6), 2081–2092.

Brune, J.N., 1970. Tectonic stress and the spectra of seismic shear waves from earthquakes, *J. geophys. Res.,* **75**(26), 4997–5009.

Clouser, R. & Langston, C., 1995. Modeling P-Rg conversions from isolated topographic features near the NORESS array, *Bull. seism. Soc. Am.,* **85**(3), 859–873.

Davies, D., Kelly, E. & Filson, J., 1971. Vespa process for analysis of seismic signals, *Nature Phys. Sci.,* **232,** 8–13.

Dodge, D. & Beroza, G., 1997. Source array analysis of coda waves near the 1989 Loma Prieta, California, mainshock: implications for the mechanism of coseismic velocity changes, *J. geophys. Res.,* **102**(B11), 24 437–24 458.

Dolan, S., Bean, C. & Riollet, B., 1998. The broad-band fractal nature of heterogeneity in the upper crust from petrophysical logs, *Geophys. J. Int.,* **132,** 489–507.

Dominguez, L.A., Davis, P.M. & Hollis, D., 2013. Application of fk analysis and entropy to track the transition from spatially coherent to incoherent earthquake coda in Long Beach, California, *Seis. Res. Lett.,* **84**(4), 622–628.

Dunham, E.M., Belanger, D., Cong, L. & Kozdon, J.E., 2011. Earthquake ruptures with strongly rate-weakening friction and off-fault plasticity, Part 2: nonplanar faults, *Bull. seism. Soc. Am.,* **101**(5), 2308–2322.

Flatté, S.M. & Wu, R.S., 1988. Small-scale structure in the lithosphere and asthenosphere deduced from arrival time and amplitude fluctuations at NORSAR, *J. geophys. Res.,* **93**(B6), 6601–6614.

Frankel, A. & Clayton, R.W., 1986. Finite-difference simulations of seismic scattering – implications for the propagation of short-period seismic-waves in the crust and models of crustal heterogeneity, *J. geophys. Res.,* **91**(B6), 6465–6489.

Frankel, A. & Wennerberg, L., 1987. Energy-flux model of seismic coda: separation of scattering and intrinsic attenuation, *Bull. seism. Soc. Am.,* **77**(4), 1223–1251.

Galis, M., Imperatori, W. & Mai, P.M., 2013. Quantitative analysis of accuracy of seismic wave-propagation codes in 3D random scattering media, *Geophys. Res. Abstr.,* **15,** EGU2013–6692.

Geli, L., Bard, P. & Jullien, B., 1988. The effect of topography on earthquake ground motion: a review and new results, *Bull. seism. Soc. Am.,* **78**(1), 42–63.

Graves, R.W. & Pitarka, A., 2010. Broadband ground-motion simulation using a hybrid approach, *Bull. seism. Soc. Am.,* **100**(5A), 2095–2123.

Guatteri, M., Mai, P.M., Beroza, G.C. & Boatwright, J., 2003. Strong ground-motion prediction from stochastic-dynamic source models, *Bull. seism. Soc. Am.,* **93**(1), 301–313.

Hartzell, S., Harmsen, S. & Frankel, A., 2010. Effects of 3D random correlated velocity perturbations on predicted ground motions, *Bull. seism. Soc. Am.,* **100**(4), 1415–1426.

Hestholm, S., Ruud, B. & Husebye, E., 1999. 3D versus 2D finite-difference seismic synthetics including real surface topography, *Phys. Earth planet. Inter.,* **113**(1), 339–354.

Holliger, K., 1997. Seismic scattering in the upper crystalline crust based on evidence from sonic logs, *Geophys. J. Int.,* **128**(1), 65–72.

Hoshiba, M., 1991. Simulation of multiple-scattered coda wave excitation based on the energy-conservation law, *Phys. Earth planet. Inter.,* **67**(1–2), 123–136.

Hoshiba, M., 1993. Separation of scattering attenuation and intrinsic absorption in Japan using the multiple lapse time window analysis of full seismogram envelope, *J. geophys. Res.,* **98**(B9), 15 809–15 824.

Hoshiba, M., 1994. Simulation of coda wave envelope in-depth dependent scattering and absorption structure, *Geophys. Res. Lett.,* **21**(25), 2853–2856.

Husen, S., Kissling, E., Deichmann, N., Wiemer, S., Giardini, D. & Baer, M., 2003. Probabilistic earthquake location in complex three-dimensional velocity models: application to Switzerland, *J. geophys. Res.,* **108**(B2), 2077, doi:10.1029/2002JB001778.

Imperatori, W. & Mai, P.M., 2012. Sensitivity of broad-band ground-motion simulations to earthquake source and Earth structure variations: an application to the Messina Straits (Italy), *Geophys. J. Int.,* **188**(3), 1103–1116.

Imperatori, W. & Mai, P.M., 2013. Broad-band near-field ground motion simulations in 3-dimensional scattering media, *Geophys. J. Int.,* **192,** 725–744.

Komatitsch, D. & Vilotte, J., 1998. The spectral element method: An efficient tool to simulate the seismic response of 2D and 3D geological structures, *Bull. seism. Soc. Am.,* **88**(2), 368–392.

Komatitsch, D., Liu, Q., Tromp, J., Suss, P., Stidham, C. & Shaw, J., 2004. Simulations of ground motion in the Los Angeles basin based upon the spectral-element method, *Bull. seism. Soc. Am.,* **94**(1), 187–206.

Kosuga, M., 1992. Dependence of coda Q on frequency and lapse time in the western Nagano region, central Japan, *J. Phys. Earth,* **40**(2), 421–445.

Kumagai, H., Saito, T., O'Brien, G. & Yamashina, T., 2011. Characterization of scattered seismic wavefields simulated in heterogeneous media with topography, *J. geophys. Res.,* **116,** B03308, doi:10.1029/2010JB007718.

Lee, S., Chen, H., Liu, Q., Komatitsch, D., Huang, B. & Tromp, J., 2008. Three-dimensional simulations of seismic-wave propagation in the Taipei basin with realistic topography based upon the spectral-element method, *Bull. seism. Soc. Am.,* **98**(1), 253–264.

Lee, S.-J., Komatitsch, D., Huang, B.-S. & Tromp, J., 2009. Effects of topography on seismic-wave propagation: an example from Northern Taiwan, *Bull. seism. Soc. Am.,* **99**(1), 314–325.

Liu, P., Archuleta, R.J. & Hartzell, S.H., 2006. Prediction of broadband ground-motion time histories: hybrid low/high-frequency method with correlated random source parameters, *Bull. seism. Soc. Am.,* **96**(6), 2118–2130.

Ma, S., Archuleta, R.J. & Page, M.T., 2007. Effects of large-scale surface topography on ground motions, as demonstrated by a study of the San Gabriel Mountains, Los Angeles, California, *Bull. seism. Soc. Am.,* **97**(6), 2066–2079.

Magnoni, F., Casarotti, E., Michelini, A., Piersanti, A., Komatitsch, D., Peter, D. & Tromp, J., 2014. Spectral-element simulations of seismic waves generated by the 2009 L'Aquila earthquake, *Bull. seism. Soc. Am.,* **104**(1), 73–94.

Mai, P.M., Imperatori, W. & Olsen, K.B., 2010. Hybrid broadband ground-motion simulations: Combining long-period deterministic synthetics with

high-frequency multiple S-to-S backscattering, *Bull. seism. Soc. Am.,* **100**(5A), 2124–2142.

Mayeda, K., Koyanagi, S., Hoshiba, M., Aki, K. & Zeng, Y.H., 1992. A comparative-study of scattering, intrinsic, and coda Q^{-1} for Hawaii, Long Valley, and central California between 1.5 Hz and 15.0 Hz, *J. geophys. Res.,* **97**(B5), 6643–6659.

Nielsen, L. & Thybo, H., 2003. The origin of teleseismic Pn waves: Multiple crustal scattering of upper mantle whispering gallery phases, *J. geophys. Res.,* **108**(B10), doi:10.1029/2003JB002487.

Nilsson, S., Petersson, N., Sjögreen, B. & Kreiss, H., 2007. Stable difference approximations for the elastic wave equation in second order formulation, *SIAM J. Num. Anal.,* **45**(5), 1902–1936.

O'Brien, G.S. & Bean, C.J., 2009. Volcano topography, structure and intrinsic attenuation: Their relative influences on a simulated 3D visco-elastic wavefield, *J. Volc. Geotherm. Res.,* **183**(1–2), 122–136.

Olsen, K.B., Day, S.M. & Bradley, C.R., 2003. Estimation of Q for long-period (>2 sec) waves in the Los Angeles basin, *Bull. seism. Soc. Am.,* **93**(2), 627–638.

Oprsal, I., FähD. Mai, P.M. & Giardini, D., 2005. Deterministic earthquake scenario for the basel area: simulating strong motions and site effects for Basel, Switzerland, *J. geophys. Res.,* **110,** B04305, doi:10.1029/2004JB003188.

Petersson, N.A. & Sjögreen, B., 2012. Stable and efficient modeling of anelastic attenuation in seismic wave propagation, *Comm. Comput. Phys.,* **12**(1), 193–225.

Pitarka, A., 2009. Simulating forward and backward scattering in viscoelastic 3D media with random velocity variations and basin structure, *Tech. rep.,* USGS, Award number 06HQGR0042.

Pitarka, A. & Irikura, K., 1996. Modeling 3D surface topography by finite difference method: Kobe JMA station site, Japan, case study, *Geophys. Res. Lett.,* **23**(20), 2729–2732.

Rautian, T. & Aki, K., 1978. The use of the coda for determination of the earthquake source spectrum, *Bull. seism. Soc. Am.,* **68**(4), 923–948.

Ripperger, J., Igel, H. & Wasserman, J., 2003. Seismic wave simulation in the presence of real volcano topography, *J. Volc. Geotherm. Res.,* **128**(1), 31–44.

Ripperger, J., Mai, P.M. & Ampuero, J.P., 2008. Variability of near-field ground motion from dynamic earthquake rupture simulations, *Bull. seism. Soc. Am.,* **98**(3), 1207–1228.

Rodgers, A., Petersson, N.A., Nilsson, S., Sjogreen, B. & McCandless, K., 2008. Broadband waveform modeling of moderate earthquakes in the San Francisco Bay area and preliminary assessment of the USGS 3D seismic velocity model, *Bull. seism. Soc. Am.,* **98**(2), 969–988.

Rodgers, A.J., Petersson, N.A. & Sjogreen, B., 2010. Simulation of topographic effects on seismic waves from shallow explosions near the North Korean nuclear test site with emphasis on shear wave generation, *J. geophys. Res.,* **115,** B11309, doi:10.1029/2010JB007707.

Rost, S. & Thomas, C., 2002. Array seismology: Methods and applications, *Rev. Geophys.,* **40**(3), doi:10.1029/2000RG000100.

Roten, D., Faeh, D., Olsen, K.B. & Giardini, D., 2008. A comparison of observed and simulated site response in the Rhone Valley, *Geophys. J. Int.,* **173**(3), 958–978.

Roth, M. & Korn, M., 1993. Single scattering-theory versus numerical modeling in 2D random-media, *Geophys. J. Int.,* **112**(1), 124–140.

Saito, T., Sato, H. & Ohtake, M., 2002. Envelope broadening of spherically outgoing waves in three-dimensional random media having power law spectra, *J. geophys. Res.,* **107**(B5), 2089, doi:10.1029/2001JB000264.

Sato, H., 1989. Broadening of seismogram envelopes in the randomly inhomogeneous lithosphere based on the parabolic approximation – southeastern Honshu, Japan, *J. geophys. Res.,* **94**(B12), 17 735–17 747.

Sato, H. & Fehler, M.C., 1998. *Seismic Wave Propagation and Scattering in the Heterogeneous Earth,* AIP Springer.

Sato, H. & Fehler, M.C., 2007. Synthesis of seismogram envelopes in heterogeneous media, *Adv. Geophys.,* **48,** 561–596.

Sato, H., Fehler, M. & Saito, T., 2004. Hybrid synthesis of scalar wave envelopes in two-dimensional random media having rich short-wavelength spectra, *J. geophys. Res.,* **109**(B6), B06303, doi:10.1029/2003JB002673.

Shakal, A., Haddadi, H., Graizer, V., Lin, K. & Huang, M., 2006. Some key features of the strong-motion data from the Mw 6.0 Parkfield, California, earthquake of 28 September 2004, *Bull. seism. Soc. Am.,* **96**(4), S90–S118.

Shi, Z. & Day, S.M., 2013. Rupture dynamics and ground motion from 3D rough-fault simulations, *J. geophys. Res.,* **118,** 1122–1141.

Spudich, P. & Bostwick, T., 1987. Studies of the seismic coda using an earthquake cluster as a deeply buried seismograph array, *J. geophys. Res.,* **92**(B10), 10 526–10 546.

Spudich, P. & Chiou, B.S.J., 2008. Directivity in NGA earthquake ground motions: analysis using isochrone theory, *Earthquake Spectra,* **24**(1), 279–298.

Spudich, P., Hellweg, M. & Lee, W.H.K., 1996. Directional topographic site response at Tarzana observed in aftershocks of the 1994 Northridge, California, earthquake: implications for mainshock motions, *Bull. seism. Soc. Am.,* **86**(1), S193–S208.

Steimen, S., Fäh, D., Kind, F., Schmid, C. & Giardini, D., 2003. Identifying 2D resonance in microtremor wave fields, *Bull. Seis. Soc. Am.,* **93**(2), 583–599.

Stupazzini, M., de la Puente, J., Smerzini, C., Kaeser, M., Igel, H. & Castellani, A., 2009. Study of rotational ground motion in the near-field region, *Bull. seism. Soc. Am.,* **99**(2B), 1271–1286.

Takemura, S. & Furumura, T., 2013. Scattering of high-frequency P wavefield derived by dense Hi-Net array observations in Japan and computer simulations of seismic wave propagations, *Geophys. J. Int.,* **193,** 421–436.

Takemura, S., Furumura, T. & Saito, T., 2009. Distortion of the apparent S-wave radiation pattern in the high-frequency wavefield: Tottori-Ken Seibu, Japan, earthquake of 2000, *Geophys. J. Int.,* **178**(2), 950–961.

Takenaka, H., Mamada, Y. & Futamure, H., 2003. Near-source effect on radiation pattern of high-frequency S waves: strong SH-SV mixing observed from aftershocks of the 1997 northwestern Kagoshima, Japan, earthquakes, *Phys. Earth planet. Inter.,* **137**(1–4), 31–43.

Tuvé, T., Bianco, F., Ibanez, J., Patane, D., Pezzo, E.D. & Bottari, A., 2006. Attenuation study in the Straits of Messina area (Southern Italy), *Tectonophysics,* **421**(3–4), 173–185.

Vernon, F., Pavlis, G., Owens, T., McNamara, D. & Anderson, P., 1998. Near-surface scattering effects observed with a high-frequency phased array at Pinyon Flats, California, *Bull. seism. Soc. Am.,* **88**(6), 1548–1560.

Wagner, G.S., 1997. Regional wave propagation in southern California and Nevada: observations from a three-component seismic array, *J. geophys. Res.,* **102**(B4), 8285–8311.

Wennerberg, L., 1993. Multiple-scattering interpretations of coda-Q measurements, *Bull. seism. Soc. Am.,* **83**(1), 279–290.

Wu, R.S., 1985. Multiple-scattering and energy-transfer of seismic-waves separation of scattering effect from intrinsic attenuation. Theoretical modeling, *Geophys. J. R. astr. Soc.,* **82**(1), 57–80.

Zeng, Y.H., 1991. Compact solutions for multiple scattered wave energy in time domain, *Bull. seism. Soc. Am.,* **81**(3), 1022–1029.

Zeng, Y.H., 1993. Theory of scattered P-wave and S-wave energy in a random isotropic scattering medium, *Bull. seism. Soc. Am.,* **83**(4), 1264–1276.

Zeng, Y.H., Su, F. & Aki, K., 1991. Scattering wave energy propagation in a random isotropic scattering medium. theory, *J. geophys. Res.,* **96**(B1), 607–619.

Zerva, A. & Zervas, V., 2002. Spatial variation of seismic ground motions: an overview, *Appl. Mech. Rev.,* **55**(3), 271–297.

Zhang, W., Shen, Y. & Chen, X., 2008. Numerical simulation of strong ground motion for the Ms8.0 Wenchuan earthquake of 12 May 2008, *Sci. China Ser. D-Earth Sci.,* **51**(12), 1673–1682.